Research Square

Preprints are preliminary reports that have not undergone peer review.
They should not be considered conclusive, used to inform clinical practice,
or referenced by the media as validated information.

Nonlinear Bloch mode synthesis for amplitude-dependent dispersion in periodic systems

Said Quqa

said.quqa2@unibo.it

University of Bologna

Antonio Palermo

University of Bologna

Research Article

Keywords: Bloch mode synthesis, Nonlinear metamaterial, Amplitude-dependent dispersion, Invariant manifold, Component mode synthesis, Reduced-order model

Posted Date: November 24th, 2026

DOI: https://doi.org/10.21203/rs.3.rs-11688655/v1

License: This work is licensed under a Creative Commons Attribution 4.0 International License.
Read Full License

Additional Declarations: No competing interests reported.

Nonlinear Bloch mode synthesis for amplitude-dependent dispersion in periodic systems

Said Quqa[1*] and Antonio Palermo[1]

[1*]Department of Civil, Chemical, Environmental and Materials Engineering, University of Bologna, Bologna, 40136, Italy.

*Corresponding author. E-mail: said.quqa2@unibo.it;

Abstract

This work proposes a nonlinear extension of Bloch mode synthesis for computing amplitude-dependent dispersion relations in nonlinear periodic structures. The approach is based on a correction of individual Bloch branches evaluated as a function of the oscillation amplitude. The unit-cell dynamics is first reduced by means of Craig-Bampton component mode synthesis, with a set of retained fixed-interface modes. Here, discarded modal coordinates are expressed as functions of the coordinates retained in the reduced model through single-master nonlinear mappings. These mappings are computed once and reused across the Brillouin zone. Bloch conditions are thus imposed on the reduced model, whose linear eigenvectors define a harmonic reference orbit for each branch and wavenumber. At each wavenumber and amplitude, the nonlinear forces are sampled along the harmonic orbit of the selected linear Bloch mode, and their fundamental component is used to obtain a scalar frequency correction through a Rayleigh quotient. The method targets isolated, weakly nonlinear branches. Its predictions agree with time-domain simulations of a finite chain.

Keywords: Bloch mode synthesis, Nonlinear metamaterial, Amplitude-dependent dispersion, Invariant manifold, Component mode synthesis, Reduced-order model

1 Introduction

Periodic elastic structures and mechanical metamaterials provide a versatile framework for controlling wave propagation through Bragg scattering, local resonances, and their interaction [1–3].

In the linear regime, Bloch-Floquet theory reduces the analysis of an infinite periodic structure to a single unit cell, whose boundary displacements are related through a phase factor that depends on the wavenumber. This leads to an eigenvalue problem in the frequency and the wavenumber, whose solutions trace the dispersion branches. When only propagating waves are of interest, the wavenumber can be prescribed as a real parameter, and a generalized eigenvalue problem in the squared frequency is solved at each wavenumber [4]. For unit cells with many degrees of freedom (DOFs), repeating this problem for many wavenumbers across the first Brillouin zone becomes expensive, which has motivated the development of reduced-order models (ROMs). Among these approaches, Bloch mode synthesis (BMS) [4] applies Craig-Bampton component mode synthesis (CMS) [5] to the unit cell: the interior is described by a truncated set of fixed-interface normal modes, which do not depend on the wavenumber, while the boundary DOFs remain physical and carry the Bloch conditions. Generalized BMS [6] adds a wavenumber-independent reduction of the boundary DOFs and residual-mode corrections for the truncated interior modes, related to the residual-flexibility enhancements of the Craig-Bampton method [7].

Geometric or material nonlinearities make the dispersion branches amplitude-dependent and can consequently shift pass-bands, stop-bands, and resonance frequencies [8]. Amplitude-dependent dispersion analysis has thus attracted particular interest in nonlinear periodic media [9]. Early studies of discrete and continuous periodic systems identified amplitude-dependent wave speeds and nonlinear transmission phenomena [10, 11]. Perturbation formulations were subsequently developed for one- and two-dimensional lattices [12, 13], followed by harmonic-balance approaches applicable beyond the leading perturbation order [14]. More recent work examined phononic crystals and locally resonant metamaterials, in which cubic nonlinearities produce amplitude-dependent band structures and tunable band gaps [15–18]. These effects have also been observed experimentally [19].

In nonlinear structural dynamics, invariant manifolds provide a convenient framework for model-order reduction. An invariant manifold is a surface in the state space of the system, described by displacements and velocities, such that any trajectory starting on it remains on it. This concept is closely related to nonlinear normal modes (NNMs), which extend the notion of linear normal modes to nonlinear systems. Originally introduced by Rosenberg [20] as synchronous oscillations of all system coordinates, NNMs were generalized by Shaw and Pierre [21] as motions confined to invariant manifolds tangent to the modal subspaces of the corresponding linearized system. In their formulation, each manifold is parametrized by the displacement and velocity of a single master modal coordinate, while the remaining (slave) coordinates are expressed as functions of these two variables. The dynamics restricted to the manifold is thus governed by a single nonlinear oscillator.

The invariant manifold formulation was subsequently extended to multiple master coordinates, allowing modal interactions and internal resonances to be represented

[22, 23]. Numerical continuation techniques further enabled the computation of NNMs in larger structural systems [24], while different invariant manifold approaches were developed for the reduced-order modeling of geometrically nonlinear structures [25, 26]. More recently, the theory of spectral submanifolds (SSMs) has provided existence and uniqueness results for certain invariant manifolds and established a framework for constructing ROMs of high-dimensional systems, including finite-element (FE) models [27–29].

More recently, invariant manifold-based model-order reduction has been applied to the analysis of amplitude-dependent dispersion in nonlinear periodic media. Wang et al. [30] employed the parametrization method for invariant manifolds, expressed in complex normal form, to derive arbitrary-order approximations of the nonlinear dispersion relations of locally resonant chains with quadratic and cubic stiffness nonlinearities, considering both conservative and underdamped systems. Their approach reduces the dynamics of a selected Bloch branch to a two-dimensional invariant manifold, without reducing the underlying unit-cell model. For each prescribed wavenumber, the manifold is constructed from the Bloch eigenpairs of the full-order cell, and its polynomial coefficients are determined order by order by solving wavenumber-dependent linear systems. The resulting formulation provides the nonlinear frequency as a function of wave amplitude, with closed-form third-order expressions for the two-DOF unit cell considered and numerical solutions at higher orders.

For elastic waveguides hosting multi-DOF nonlinear resonators, Quqa et al. [31] employed invariant manifolds to reduce the resonator dynamics and an effective-medium formulation to describe their coupling with the host waveguide. This approach requires an analytical solution for the host waveguide and cannot, in general, be extended to arbitrary discrete periodic systems.

Building on these developments, this work combines the principles of BMS and invariant manifold-based reduction to develop an efficient approach for computing amplitude-dependent dispersion relations in nonlinear periodic structures. As in linear BMS, a Craig-Bampton transformation describes the cell interior through fixed-interface modal coordinates, while the boundary DOFs remain physical. Only a subset of modal coordinates is retained, and the equations of the remaining (slave) coordinates are removed. The Bloch conditions are then imposed on the boundary DOFs of the linear reduced model, whose eigenproblem provides the linear dispersion relations and the Bloch modes. The nonlinear forces are then computed with the slave coordinates reconstructed from the retained ones, through mappings inspired by the invariant-manifold construction of Shaw and Pierre [21] in the Galerkin form of Pesheck et al. [32]. These forces are evaluated along the harmonic orbit of a linear Bloch mode, and their fundamental component, projected onto that mode, corrects the frequency through a Rayleigh quotient.

The mappings are computed once, on the cell interior with the interface held fixed, and, like the fixed-interface modes of BMS, do not depend on the wavenumber. Nonlinear equations are thus solved only in this preliminary stage. At a prescribed amplitude, the sweep over wavenumber requires only the linear eigenproblem of the reduced cell, the evaluation of the forces over one period, and a scalar projection.

The formulation also includes criteria for selecting the retained modes along each dispersion branch, together with a detuning criterion to identify and promote slave modes approaching internal resonance with the retained modes (at 1:1 and 3:1 frequency ratios for the cubic nonlinearity considered here).

The results are compared with direct time integration of the unit cell, with a full-order harmonic balance, and with time-domain simulations of a finite chain. The contribution of each step in the proposed procedure is also assessed by comparing three levels of treatment of the discarded coordinates in the projected forces: (i) truncation, as in conventional BMS; (ii) inclusion of their first-order response through residual flexibility [6]; and (iii) additional reconstruction of their nonlinear response, which accounts for the nonlinear interaction between retained and discarded modes in both the nonlinear and the inertial forces.

The remainder of the paper is organized as follows: Section 2 presents the nonlinear BMS formulation; Section 3 quantifies the computational complexity and compares it against the harmonic balance method; Section 4 introduces the criteria for selecting the retained modes; Section 5 applies the method to a locally resonant unit cell, compares the three levels of treatment of the discarded coordinates with direct time integration, and assesses the dominant-master assumption through modal participation and nonlinear activation; Section 6 validates the predicted amplitude-dependent wavenumbers against time-domain simulations of a finite chain and a full-order harmonic balance; Section 7 summarizes the main findings.

2 Methodology

Consider a nonlinear periodic structure consisting of identical unit cells of length a, repeated along one spatial direction. Each unit cell is discretized using, for instance, finite elements or lumped masses and springs. In the linear regime, wave propagation is governed by Bloch's theorem, whereby the response of adjacent cells differs by a phase shift qa, with q denoting the wavenumber. The dispersion relation is then described by a set of branches $\omega_n(q)$, where n denotes the branch index and $q \in [-\pi/a, \pi/a]$ spans the first Brillouin zone. In the nonlinear regime, the wave frequency also depends on the oscillation amplitude, generating amplitude-dependent dispersion relations.

This section presents an approximate procedure to determine the amplitude-dependent frequency $\widetilde{\omega}_n(q, A)$ of a selected branch n, where A is a suitable amplitude measure introduced below. The procedure consists of five steps. The first three are performed once, in a *preliminary* stage, and do not depend on the wavenumber:

1. The equation of motion of the cell is written in Craig-Bampton coordinates, in which the internal displacements are represented by fixed-interface and constraint modes, while the boundary DOFs remain physical. A subset of fixed-interface modes is retained, and the equations of the slave modes are removed (Section 2.1).
2. The first-order slave response is expressed through residual flexibility, which recovers the linear inertial coupling between the slave coordinates and the boundary (Section 2.2).

3. The higher-order slave response is reconstructed from the retained coordinates through single-master mappings based on invariant manifolds, computed on the fixed-interface internal subsystem (Section 2.3).

The last two steps form the *evaluation* stage, the first conducted for each wavenumber and the second for each wavenumber and amplitude of interest:

4. The Bloch conditions are imposed on the boundary DOFs of the first-order reduced model, and a residual-enhanced eigenproblem of reduced size provides the linear dispersion relation and the Bloch modes (Section 2.4).
5. The nonlinear forces, evaluated with the reconstructed slave coordinates along a harmonic orbit prescribed by the selected Bloch mode, are projected onto the fundamental harmonic and the Bloch mode, which yields a scalar correction to the frequency (Section 2.5).

2.1 Model order reduction via Craig-Bampton transformation

Before the Bloch reduction is applied, the equation of motion of one cell reads

$$\mathbf{M}\ddot{\mathbf{u}} + \mathbf{K}\mathbf{u} + \mathbf{g}(\mathbf{u}) = \mathbf{f}, \tag{1}$$

where $\mathbf{u} \in \mathbb{R}^N$ collects the displacements, $\mathbf{M}$ and $\mathbf{K}$ are the mass and linear stiffness matrices, $\mathbf{g}(\mathbf{u})$ is the nonlinear restoring-force vector, and $\mathbf{f}$ contains the interface tractions exerted by the neighboring cells. DOFs shared by adjacent cells are termed *boundary* DOFs, and all remaining DOFs are *internal*.

The formulation rests on the following assumptions:

(i) The system is undamped and is not subject to external loads, so that $\mathbf{f}$ contains only intercell tractions.
(ii) The nonlinear force depends only on the displacements and is conservative, i.e., it derives from a potential energy. Its tangent $\partial\mathbf{g}/\partial\mathbf{u}$ is thus symmetric.
(iii) Each nonlinear element is contained within one cell and acts only on internal DOFs. Nonlinear elements that cross the cell boundary are not considered.
(iv) The nonlinearity is weak and odd, $\mathbf{g}(-\mathbf{u}) = -\mathbf{g}(\mathbf{u})$, so that its leading effect on the frequency appears in the fundamental harmonic of the force evaluated along a linear Bloch orbit, and the motion remains dominated by this harmonic on a single, isolated Bloch branch. For simplicity, the specific workflow and the examples consider cubic nonlinearities.

Equation (1) can be rewritten by partitioning internal (i) and boundary (b) components,

$$\mathbf{u} = \begin{bmatrix} \mathbf{u}_\mathrm{i} \\ \mathbf{u}_\mathrm{b} \end{bmatrix}, \tag{2}$$

with $\mathbf{u}_\mathrm{i} \in \mathbb{R}^{N_\mathrm{i}}$ and $\mathbf{u}_\mathrm{b} \in \mathbb{R}^{N_\mathrm{b}}$, where $N = N_\mathrm{i} + N_\mathrm{b}$, leading to the block form

$$\begin{bmatrix} \mathbf{M}_\mathrm{ii} & \mathbf{M}_\mathrm{ib} \\ \mathbf{M}_\mathrm{bi} & \mathbf{M}_\mathrm{bb} \end{bmatrix} \begin{bmatrix} \ddot{\mathbf{u}}_\mathrm{i} \\ \ddot{\mathbf{u}}_\mathrm{b} \end{bmatrix} + \begin{bmatrix} \mathbf{K}_\mathrm{ii} & \mathbf{K}_\mathrm{ib} \\ \mathbf{K}_\mathrm{bi} & \mathbf{K}_\mathrm{bb} \end{bmatrix} \begin{bmatrix} \mathbf{u}_\mathrm{i} \\ \mathbf{u}_\mathrm{b} \end{bmatrix} + \begin{bmatrix} \mathbf{g}_\mathrm{i}(\mathbf{u}) \\ \mathbf{0} \end{bmatrix} = \begin{bmatrix} \mathbf{0} \\ \mathbf{f}_\mathrm{b} \end{bmatrix}. \tag{3}$$

A Craig-Bampton transformation [5] is introduced. The internal displacements are represented by the superposition of fixed-interface normal modes, with modal coordinates $\boldsymbol{\eta}$ (entries η_m, $m = 1, \ldots, N_\mathrm{i}$), and constraint modes describing the static internal response to unit boundary displacements. Collecting the two sets of coordinates in the mixed modal-physical vector

$$\widehat{\mathbf{u}} = \begin{bmatrix} \boldsymbol{\eta} \\ \mathbf{u}_\mathrm{b} \end{bmatrix}, \tag{4}$$

the transformation reads

$$\mathbf{u} = \mathbf{T}\widehat{\mathbf{u}}, \qquad \mathbf{T} = \begin{bmatrix} \boldsymbol{\Phi} & \boldsymbol{\Psi} \\ \mathbf{0} & \mathbf{I}_{N_\mathrm{b}} \end{bmatrix}. \tag{5}$$

Here, $\boldsymbol{\Phi}$ contains the fixed-interface normal modes obtained from

$$\mathbf{K}_\mathrm{ii}\boldsymbol{\Phi} = \mathbf{M}_\mathrm{ii}\boldsymbol{\Phi}\boldsymbol{\Omega}^2, \tag{6}$$

with the normalization $\boldsymbol{\Phi}^\mathsf{T}\mathbf{M}_\mathrm{ii}\boldsymbol{\Phi} = \mathbf{I}$, so that $\boldsymbol{\Phi}^\mathsf{T}\mathbf{K}_\mathrm{ii}\boldsymbol{\Phi} = \boldsymbol{\Omega}^2$. The constraint-mode matrix is

$$\boldsymbol{\Psi} = -\mathbf{K}_\mathrm{ii}^{-1}\mathbf{K}_\mathrm{ib}. \tag{7}$$

Substituting Equation (5) into Equation (3) and projecting onto the Craig-Bampton basis yields

$$\widehat{\mathbf{M}}\ddot{\widehat{\mathbf{u}}} + \widehat{\mathbf{K}}\widehat{\mathbf{u}} + \widehat{\mathbf{g}}(\widehat{\mathbf{u}}) = \widehat{\mathbf{f}}, \tag{8}$$

with

$$\widehat{\mathbf{M}} = \mathbf{T}^\mathsf{T}\mathbf{M}\mathbf{T}, \qquad \widehat{\mathbf{K}} = \mathbf{T}^\mathsf{T}\mathbf{K}\mathbf{T}, \qquad \widehat{\mathbf{g}}(\widehat{\mathbf{u}}) = \mathbf{T}^\mathsf{T}\mathbf{g}(\mathbf{T}\widehat{\mathbf{u}}), \qquad \widehat{\mathbf{f}} = \mathbf{T}^\mathsf{T}\mathbf{f} = \mathbf{f}. \tag{9}$$

Here, the symbol $\widehat{\square}$ denotes quantities expressed in the mixed modal-physical coordinates $\widehat{\mathbf{u}}$ of Equation (4).

Notably, in this formulation, the boundary coordinates are retained in physical form and remain available for imposing the Bloch conditions, as detailed in Section 2.4.

The model of Equation (8) is then reduced by retaining only a subset of the fixed-interface modes. Accordingly, the internal modal vector is split into retained (master) and slave coordinates,

$$\boldsymbol{\eta} = \begin{bmatrix} \boldsymbol{\eta}_\mathrm{r} \\ \boldsymbol{\eta}_\mathrm{s} \end{bmatrix}, \tag{10}$$

with $\boldsymbol{\eta}_\mathrm{r} \in \mathbb{R}^{N_\mathrm{r}}$, $\boldsymbol{\eta}_\mathrm{s} \in \mathbb{R}^{N_\mathrm{s}}$, $N_\mathrm{s} = N_\mathrm{i} - N_\mathrm{r}$, and index sets $\mathcal{R}$ and $\mathcal{S}$. The fixed-interface modes and their eigenvalues are thus partitioned as:

$$\boldsymbol{\Phi} = \begin{bmatrix} \boldsymbol{\Phi}_\mathrm{r} & \boldsymbol{\Phi}_\mathrm{s} \end{bmatrix}, \quad \boldsymbol{\Omega}^2 = \begin{bmatrix} \boldsymbol{\Omega}_\mathrm{r}^2 & \mathbf{0} \\ \mathbf{0} & \boldsymbol{\Omega}_\mathrm{s}^2 \end{bmatrix}. \tag{11}$$

In a conventional linear Craig-Bampton reduction, the slave rows and columns are deleted, which is equivalent to setting $\boldsymbol{\eta}_\mathrm{s} = \mathbf{0}$. Here, only the retained and boundary

rows of Equation (8) are included in the reduced governing equations, yielding a system of $N_\mathrm{r} + N_\mathrm{b}$ equations. The slave equations are instead used separately to reconstruct their contributions to the reduced model, as detailed below. Since $\widehat{\mathbf{M}}_\mathrm{rs} = \mathbf{0}$ and $\widehat{\mathbf{K}}_\mathrm{rs} = \widehat{\mathbf{K}}_\mathrm{rb} = \widehat{\mathbf{K}}_\mathrm{bs} = \mathbf{0}$ by Equations (6) and (7), the retained and boundary rows of Equation (8) read

$$\underbrace{\begin{bmatrix} \mathbf{I}_{N_\mathrm{r}} & \widehat{\mathbf{M}}_\mathrm{rb} \\ \widehat{\mathbf{M}}_\mathrm{br} & \widehat{\mathbf{M}}_\mathrm{bb} \end{bmatrix}}_{\overline{\mathbf{M}}} \begin{bmatrix} \ddot{\boldsymbol{\eta}}_\mathrm{r} \\ \ddot{\mathbf{u}}_\mathrm{b} \end{bmatrix} + \underbrace{\begin{bmatrix} \mathbf{0} \\ \widehat{\mathbf{M}}_\mathrm{bs} \end{bmatrix}}_{\overline{\mathbf{f}}_\mathrm{in}} \ddot{\boldsymbol{\eta}}_\mathrm{s} + \underbrace{\begin{bmatrix} \boldsymbol{\Omega}_\mathrm{r}^2 & \mathbf{0} \\ \mathbf{0} & \widehat{\mathbf{K}}_\mathrm{bb} \end{bmatrix}}_{\overline{\mathbf{K}}} \begin{bmatrix} \boldsymbol{\eta}_\mathrm{r} \\ \mathbf{u}_\mathrm{b} \end{bmatrix} + \underbrace{\begin{bmatrix} \widehat{\mathbf{g}}_\mathrm{r}(\widehat{\mathbf{u}}) \\ \widehat{\mathbf{g}}_\mathrm{b}(\widehat{\mathbf{u}}) \end{bmatrix}}_{\overline{\mathbf{g}}} = \begin{bmatrix} \mathbf{0} \\ \mathbf{f}_\mathrm{b} \end{bmatrix}. \tag{12}$$

Here, the symbol $\overline{\square}$ denotes quantities of the reduced model.

The slave coordinates still enter Equation (12) through two terms: the inertial coupling $\overline{\mathbf{f}}_\mathrm{in}$ between the boundary rows and the slave accelerations, and the nonlinear force $\overline{\mathbf{g}}$.

Since the nonlinear restoring force $\mathbf{g}$ is an odd polynomial and the linear stiffness is already included in $\mathbf{K}$, $\mathbf{g}$ (and thus also $\overline{\mathbf{g}}$) has no linear term. Its leading contribution is thus of degree three. Let A denote a small amplitude parameter, later identified with the modal amplitude of the selected Bloch mode. The displacement response can be formally expanded as

$$\widehat{\mathbf{u}} = \widehat{\mathbf{u}}^{(1)} + \widehat{\mathbf{u}}^{(3)} + O(A^5), \tag{13}$$

with $\widehat{\mathbf{u}}^{(1)} = O(A)$ and $\widehat{\mathbf{u}}^{(3)} = O(A^3)$. Consequently, $\overline{\mathbf{g}}(\widehat{\mathbf{u}}) = O(A^3)$.

The first-order slave response, to which $\overline{\mathbf{g}}$ does not contribute, is expressed in Section 2.2, and the third-order slave response in Section 2.3. The Bloch conditions are then imposed at first order to obtain the linear dispersion relation (Section 2.4), and third-order effects are accounted for through an amplitude-dependent correction to the dispersion relation (Section 2.5).

2.2 First-order slave response and inertial correction

In the original CMS formulation, the inertial coupling is discarded together with the slave coordinates [4]. This truncation stiffens the reduced model and shifts the branches upward [6]. Here, $\overline{\mathbf{f}}_\mathrm{in}$ is retained through the residual-flexibility formulation of Krattiger and Hussein [6] and Kim et al. [7], so that the linear truncation error does not mask the error introduced by the treatment of the nonlinear force. At first order, the slave rows of Equation (8) give

$$\ddot{\boldsymbol{\eta}}_\mathrm{s}^{(1)} + \boldsymbol{\Omega}_\mathrm{s}^2 \, \boldsymbol{\eta}_\mathrm{s}^{(1)} + \widehat{\mathbf{M}}_\mathrm{sb} \, \ddot{\mathbf{u}}_\mathrm{b} = \mathbf{0}, \tag{14}$$

If the cell is excited by a harmonic motion of frequency ω (which is the case of interest as discussed in Section 2.4), the steady-state response of Equation (14) is [6, 7]:

$$\boldsymbol{\eta}_\mathrm{s}^{(1)} = \omega^2 (\boldsymbol{\Omega}_\mathrm{s}^2 - \omega^2 \mathbf{I})^{-1} \widehat{\mathbf{M}}_\mathrm{sb} \mathbf{u}_\mathrm{b}, \tag{15}$$

where $\widehat{\mathbf{M}}_\mathrm{sb} = \boldsymbol{\Phi}_\mathrm{s}^\mathsf{T} \mathbf{W}$ (with $\mathbf{W} = \mathbf{M}_\mathrm{ii} \boldsymbol{\Psi} + \mathbf{M}_\mathrm{ib}$) is the inertial coupling between the boundary acceleration and the slave coordinates. Substituting this response into the

inertial term of Equation (12) gives

$$\overline{\mathbf{f}}_{\mathrm{in}}(\mathbf{u}_{\mathrm{b}}) = -\omega^4 \begin{bmatrix} \mathbf{0} \\ \widehat{\mathbf{M}}_{\mathrm{bs}}(\boldsymbol{\Omega}_{\mathrm{s}}^2 - \omega^2\mathbf{I})^{-1}\widehat{\mathbf{M}}_{\mathrm{sb}}\mathbf{u}_{\mathrm{b}} \end{bmatrix}. \tag{16}$$

When the slave frequencies are well above ω, the inverse can be expanded in powers of ω^2,

$$(\boldsymbol{\Omega}_{\mathrm{s}}^2 - \omega^2\mathbf{I})^{-1} = \boldsymbol{\Omega}_{\mathrm{s}}^{-2} + \omega^2\boldsymbol{\Omega}_{\mathrm{s}}^{-4} + \dots, \tag{17}$$

and the spectral decomposition of $\mathbf{K}_{\mathrm{ii}}^{-1}$ allows the first two terms to be expressed through the retained modes only, exploiting the concept of residual flexibility [6, 7]:

$$\begin{aligned} \boldsymbol{\Phi}_{\mathrm{s}}\boldsymbol{\Omega}_{\mathrm{s}}^{-2}\boldsymbol{\Phi}_{\mathrm{s}}^{\mathsf{T}} &= \mathbf{F}_{\mathrm{res}} = \mathbf{K}_{\mathrm{ii}}^{-1} - \boldsymbol{\Phi}_{\mathrm{r}}\boldsymbol{\Omega}_{\mathrm{r}}^{-2}\boldsymbol{\Phi}_{\mathrm{r}}^{\mathsf{T}}, \\ \boldsymbol{\Phi}_{\mathrm{s}}\boldsymbol{\Omega}_{\mathrm{s}}^{-4}\boldsymbol{\Phi}_{\mathrm{s}}^{\mathsf{T}} &= \mathbf{F}_{\mathrm{res}}\mathbf{M}_{\mathrm{ii}}\mathbf{F}_{\mathrm{res}}, \end{aligned} \tag{18}$$

which yields the approximation:

$$\overline{\mathbf{f}}_{\mathrm{in}}(\mathbf{u}_{\mathrm{b}}) \approx -\omega^4 \begin{bmatrix} \mathbf{0} \\ \left(\mathbf{H}_1 + \omega^2\mathbf{H}_2\right)\mathbf{u}_{\mathrm{b}} \end{bmatrix}, \tag{19}$$

with

$$\begin{aligned} \mathbf{H}_1 &= \mathbf{W}^{\mathsf{T}}\mathbf{F}_{\mathrm{res}}\mathbf{W}, \\ \mathbf{H}_2 &= \mathbf{W}^{\mathsf{T}}\mathbf{F}_{\mathrm{res}}\mathbf{M}_{\mathrm{ii}}\mathbf{F}_{\mathrm{res}}\mathbf{W}. \end{aligned} \tag{20}$$

Notably, the $N_{\mathrm{b}} \times N_{\mathrm{b}}$ matrices $\mathbf{H}_1$ and $\mathbf{H}_2$ require only the retained modes and the factorization of $\mathbf{K}_{\mathrm{ii}}$ already used in Equation (7), while accounting for all the slave modes.

2.3 Higher-order slave response

At third order, the nonlinear force $\overline{\mathbf{g}}$ of Equation (12) contributes to the reduced equations. Since this force depends on the complete coordinate vector $\widehat{\mathbf{u}}$, its evaluation requires the slave coordinates $\boldsymbol{\eta}_{\mathrm{s}}$, which are not retained in the reduced model. In addition to their first-order response (Section 2.2), their higher-order response must thus be reconstructed from the retained coordinates.

In principle, this reconstruction can be achieved through a multi-master invariant manifold, expressing the slave coordinates as joint functions of all retained positions and velocities [22, 23]. For a nonlinearity of degree p, the corresponding reconstruction can be approximated by a homogeneous polynomial of degree p, containing both pure terms associated with individual masters and mixed terms coupling different masters.

Consider a motion of the cell, such as the Bloch modes of Section 2.4, in which one fixed-interface coordinate η_m dominates (see Section 5.2 for more details). Denoting its characteristic amplitude by A_m, assume that the remaining fixed-interface master coordinates have amplitudes of order ϵA_m, with $\epsilon \ll 1$. A polynomial term of degree p containing j factors associated with secondary masters then scales as

$$O\left(A_m^{p-j}(\epsilon A_m)^j\right) = O\left(\epsilon^j A_m^p\right), \qquad j = 0, \dots, p. \tag{21}$$

Consequently, relative to the pure dominant term, mixed terms scale as $\epsilon, \ldots, \epsilon^{p-1}$, whereas terms involving only secondary masters scale as ϵ^p. To leading order, each η_s can thus be reconstructed from the dominant master alone, through a single-master mapping, e.g., by the invariant-manifold construction of Pesheck et al. [32]. Here, this approach is followed to compute the mappings of the fixed-interface internal subsystem in the form:

$$\eta_s = X_s^{(m)}(\eta_m, \dot{\eta}_m), \qquad s \in \mathcal{S}, \tag{22}$$

where m denotes the dominant master.

The mappings are obtained from the formulation of the invariant manifold of Shaw and Pierre [21], in the Galerkin form of Pesheck et al. [32], with two changes that follow from the rest of the procedure. In that formulation, the slave displacements and velocities are expressed as functions of the amplitude and phase of the master, which evolve under the nonlinear modal force acting on the master, and the invariance conditions are projected onto a set of basis functions over a prescribed amplitude domain. Here, (i) the master motion is prescribed as linear and harmonic, consistent with the reference orbit used for the frequency correction (Section 2.5); and (ii) with this prescribed motion, the slave velocities follow directly from the slave displacements and are eliminated from the evaluation, since only the displacements enter the reconstructed nonlinear force.

With the boundary coordinates fixed at $\mathbf{u}_\mathrm{b} = \mathbf{0}$, the internal block of Equation (8) becomes

$$\ddot{\boldsymbol{\eta}} + \boldsymbol{\Omega}^2 \boldsymbol{\eta} + \widehat{\mathbf{g}}_\mathrm{i}(\boldsymbol{\eta}) = \mathbf{0}, \tag{23}$$

where $\boldsymbol{\Omega}^2 = \mathrm{diag}(\omega_1^2, \ldots, \omega_{N_\mathrm{i}}^2)$ contains the fixed-interface eigenvalues and $\widehat{\mathbf{g}}_\mathrm{i}$ is the nonlinear force projected onto the fixed-interface modes.

For a selected master m, the polar variables

$$\eta_m = \rho \cos\theta, \qquad \dot{\eta}_m = -\rho\, \omega_m \sin\theta \tag{24}$$

define the amplitude ρ and the phase θ of the master in its normalized phase plane [32].

Each slave displacement η_s is written as a function $X_s^{(m)}(\eta_m, \dot{\eta}_m)$. Here, the master motion is prescribed so that $\dot{\rho} = 0$ and $\dot{\theta} = \omega_m$. This gives $\dot{\eta}_s = \omega_m\, \partial X_s^{(m)}/\partial\theta$, which replaces the independent velocity function in Pesheck et al. [32], and $\ddot{\eta}_s = \omega_m^2\, \partial^2 X_s^{(m)}/\partial\theta^2$. The s-th row of Equation (23) then becomes

$$\omega_m^2 \frac{\partial^2 X_s^{(m)}}{\partial\theta^2} + \omega_s^2\, X_s^{(m)} + \widehat{g}_s = 0, \tag{25}$$

where $\widehat{g}_s$ is evaluated on the state with master displacement η_m and reconstructed slave displacements $X_s^{(m)}$.

In place of the polynomial-harmonic basis of Pesheck et al. [32], the mapping is expanded in homogeneous monomials of degree p of the master displacement and

normalized velocity,

$$X_s^{(m)}(\eta_m, \dot{\eta}_m) = \sum_{\xi+\zeta=p} C_{\xi\zeta}^{(s,m)}\, \eta_m^{\xi}\, (\dot{\eta}_m/\omega_m)^{\zeta}. \tag{26}$$

The coefficients $C_{\xi\zeta}^{(s,m)}$ are obtained by a Galerkin projection of Equation (25): the residual of the equation, evaluated with the expansion of Equation (26), is required to be orthogonal to each monomial of the basis over the domain $[0, \rho_{m,\max}] \times [0, 2\pi]$, with integrals computed by Gauss-Legendre quadrature in ρ and uniform quadrature in θ. Since $\widehat{g}_s$ is evaluated on the reconstructed state, the projected equations are nonlinear in the coefficients and are solved by fixed-point iteration with under-relaxation, starting from $X_s^{(m)} = 0$. Retaining only a homogeneous basis of degree p while minimizing the residual over the whole domain introduces an approximation of higher-order effects that depends on the fitting radius $\rho_{m,\max}$. This radius is chosen to encompass the master-coordinate trajectories reached in the evaluation stage (Section 2.5), which targets the reconstruction to the intended operating range.

Since the fixed-interface modes are linearly uncoupled and the boundary is held fixed, the slave coordinates are not excited at first order in the master amplitude, and the mappings are tangent to the master modal plane. With the basis of Equation (26), they contain homogeneous terms of degree p and therefore scale as $O(A_m^p)$. In the complete cell, they approximate the order-p contribution of the masters to the slave response, whereas the linear part driven by the boundary motion is accounted for separately (Section 2.2). For the cubic nonlinearity considered here, $p = 3$.

Notably, the dominant master generally varies across dispersion branches and wavenumbers (see Section 5.2). Applying Equation (22) would thus require identifying the dominant master for each Bloch mode. This can be avoided by adding to the first-order response the sum of the mappings of all retained masters:

$$\eta_s \approx \eta_s^{(1)} + \sum_{m\in\mathcal{R}} X_s^{(m)}(\eta_m, \dot{\eta}_m), \qquad s \in \mathcal{S}. \tag{27}$$

Under the dominance assumption introduced above, this sum always includes the leading contribution of order $O(A_m^p)$, regardless of which master dominates. The additional single-master contributions are of order $O(\epsilon^p A_m^p)$, whereas the neglected mixed terms have a leading order of $O(\epsilon A_m^p)$. Therefore, the additive reconstruction preserves the leading-order approximation without requiring the dominant master to be identified explicitly.

Collecting the N_s scalar relations of Equation (27) row by row defines

$$\boldsymbol{\eta}_\mathrm{s} \approx \boldsymbol{\eta}_\mathrm{s}^{(1)} + \boldsymbol{\mathcal{X}}(\boldsymbol{\eta}_\mathrm{r}, \dot{\boldsymbol{\eta}}_\mathrm{r}), \qquad \left[\boldsymbol{\mathcal{X}}(\boldsymbol{\eta}_\mathrm{r}, \dot{\boldsymbol{\eta}}_\mathrm{r})\right]_s = \sum_{m\in\mathcal{R}} X_s^{(m)}(\eta_m, \dot{\eta}_m). \tag{28}$$

Since a mapping must be constructed for each considered pair of master and slave modes, for large models the reconstruction can be restricted to a subset $\mathcal{S}_\mathrm{c} \subseteq \mathcal{S}$ of $N_\mathrm{c} \leq N_\mathrm{s}$ slave modes, setting $[\boldsymbol{\mathcal{X}}]_s = 0$ for $s \notin \mathcal{S}_\mathrm{c}$. The columns of $\boldsymbol{\Phi}_\mathrm{s}$ and the entries

of $\boldsymbol{\mathcal{X}}$ associated with $\mathcal{S}_\mathrm{c}$ are denoted by $\boldsymbol{\Phi}_\mathrm{c}$ and $\boldsymbol{\mathcal{X}}_\mathrm{c}$. This subset must include at least the slave modes up to about p times the highest retained frequency for a nonlinearity of degree p, so that the detuning screen of Section 4 can be applied.

2.4 First-order Bloch formulation

Bloch periodicity is then imposed on the first-order reduced model. Consider the reduced coordinate vector

$$\overline{\mathbf{u}} = \begin{bmatrix} \boldsymbol{\eta}_\mathrm{r} \\ \mathbf{u}_\mathrm{b}^\mathrm{L} \\ \mathbf{u}_\mathrm{b}^\mathrm{R} \end{bmatrix}, \tag{29}$$

where $\mathbf{u}_\mathrm{b}^\mathrm{L} \in \mathbb{R}^{N_\mathrm{L}}$ and $\mathbf{u}_\mathrm{b}^\mathrm{R} \in \mathbb{R}^{N_\mathrm{R}}$ denote corresponding DOFs on the left and right cell boundaries. Thus, $\mathbf{u}_\mathrm{b} = [(\mathbf{u}_\mathrm{b}^\mathrm{L})^\mathsf{T}, (\mathbf{u}_\mathrm{b}^\mathrm{R})^\mathsf{T}]^\mathsf{T}$ and $N_\mathrm{b} = N_\mathrm{L} + N_\mathrm{R}$. Corresponding meshes imply $N_\mathrm{L} = N_\mathrm{R}$.

Bloch periodicity enforces the relation

$$\mathbf{u}_\mathrm{b}^\mathrm{R} = \lambda\, \mathbf{u}_\mathrm{b}^\mathrm{L}, \qquad \lambda = e^{\mathrm{j}qa}, \tag{30}$$

where j is the imaginary unit.

The reduced coordinates satisfying Bloch periodicity are expressed as

$$\overline{\mathbf{u}} = \overline{\mathbf{B}}_q\, \overline{\mathbf{u}}_q, \qquad \overline{\mathbf{u}}_q = \begin{bmatrix} \boldsymbol{\eta}_\mathrm{r} \\ \mathbf{u}_\mathrm{b}^\mathrm{L} \end{bmatrix}, \tag{31}$$

where $\overline{\mathbf{u}}_q \in \mathbb{C}^{N_\mathrm{r}+N_\mathrm{L}}$ collects the independent Bloch coordinates and the Bloch reduction operator $\overline{\mathbf{B}}_q$ is given explicitly by

$$\overline{\mathbf{B}}_q = \begin{bmatrix} \mathbf{I}_{N_\mathrm{r}} & \mathbf{0} \\ \mathbf{0} & \mathbf{I}_{N_\mathrm{L}} \\ \mathbf{0} & \lambda\, \mathbf{I}_{N_\mathrm{L}} \end{bmatrix}, \tag{32}$$

whose last block row enforces the relation between the right and left boundary coordinates. Consistent projection of the interface tractions gives [33]:

$$\overline{\mathbf{f}} = \begin{bmatrix} \mathbf{0}_{N_\mathrm{r}} \\ \mathbf{f}_\mathrm{b}^\mathrm{L} \\ \mathbf{f}_\mathrm{b}^\mathrm{R} \end{bmatrix} \in \mathbb{C}^{N_\mathrm{r}+2N_\mathrm{L}}, \qquad \overline{\mathbf{B}}_q^\mathsf{H} \overline{\mathbf{f}} = \begin{bmatrix} \mathbf{0}_{N_\mathrm{r}} \\ \mathbf{f}_\mathrm{b}^\mathrm{L} + \lambda^* \mathbf{f}_\mathrm{b}^\mathrm{R} \end{bmatrix} = \mathbf{0}_{N_\mathrm{r}+N_\mathrm{L}}. \tag{33}$$

Without the residual-flexibility term of Equation (19), the Bloch projection of Equation (12) gives, for each wavenumber q, the generalized eigenproblem

$$\left(\overline{\mathbf{K}}_q - \omega^2 \overline{\mathbf{M}}_q\right) \boldsymbol{\varphi} = \mathbf{0}, \tag{34}$$

where the Bloch-reduced linear operators are obtained by projecting the reduced operators of Equation (12):

$$\overline{\mathbf{M}}_q = \overline{\mathbf{B}}_q^\mathsf{H}\, \overline{\mathbf{M}}\, \overline{\mathbf{B}}_q, \qquad \overline{\mathbf{K}}_q = \overline{\mathbf{B}}_q^\mathsf{H}\, \overline{\mathbf{K}}\, \overline{\mathbf{B}}_q, \tag{35}$$

and ^{H} denotes the Hermitian transpose.

Including the residual-flexibility contribution of Equation (19), the Bloch eigenproblem becomes

$$\left(\overline{\mathbf{K}}_q - \omega^2\overline{\mathbf{M}}_q - \omega^4\overline{\mathbf{H}}_{1,q} - \omega^6\overline{\mathbf{H}}_{2,q}\right)\boldsymbol{\varphi} = \mathbf{0}, \tag{36}$$

where

$$\overline{\mathbf{H}}_{k,q} = \overline{\mathbf{B}}_q^{\mathsf{H}} \begin{bmatrix} \mathbf{0} & \mathbf{0} \\ \mathbf{0} & \mathbf{H}_k \end{bmatrix} \overline{\mathbf{B}}_q. \tag{37}$$

Equation (36) is a polynomial eigenvalue problem of degree three in ω^2. Following Krattiger and Hussein [6], the frequency dependence is approximated using $\omega^2\boldsymbol{\varphi} \approx \mathbf{Y}\boldsymbol{\varphi}$, where $\mathbf{Y} = \overline{\mathbf{M}}_q^{-1}\overline{\mathbf{K}}_q$ is obtained from the operators of Equation (35). An approximation of the polynomial problem then yields the generalized eigenproblem

$$\left(\overline{\mathbf{K}}_{\mathrm{e},q} - \omega^2\overline{\mathbf{M}}_{\mathrm{e},q}\right)\boldsymbol{\varphi} = \mathbf{0}, \tag{38}$$

with

$$\begin{aligned} \overline{\mathbf{K}}_{\mathrm{e},q} &= \overline{\mathbf{K}}_q + \mathbf{Y}^{\mathsf{H}}\overline{\mathbf{H}}_{1,q}\mathbf{Y}, \\ \overline{\mathbf{M}}_{\mathrm{e},q} &= \overline{\mathbf{M}}_q + \overline{\mathbf{H}}_{1,q}\mathbf{Y} + \mathbf{Y}^{\mathsf{H}}\overline{\mathbf{H}}_{1,q} + \mathbf{Y}^{\mathsf{H}}\overline{\mathbf{H}}_{2,q}\mathbf{Y}. \end{aligned} \tag{39}$$

This eigenvalue problem has the same size as Equation (34). Its eigenvector $\boldsymbol{\varphi}$ defines the Bloch mode shape associated with the frequency $\omega_n(q)$ of branch n. Hereafter, the branch index and explicit dependence on q are omitted for brevity.

2.5 Higher-order dispersion correction

Once the linear dispersion relation has been obtained from Equation (38), the nonlinear force $\overline{\mathbf{g}}$ of Equation (12) is reintroduced to define a third-order correction term. Using the approximation of Equation (28), the nonlinear force can be evaluated as:

$$\overline{\mathbf{g}} \approx \overline{\mathbf{T}}^{\mathsf{T}}\mathbf{g}(\mathbf{u}_{\mathrm{rec}}), \tag{40}$$

where $\overline{\mathbf{T}}$ is the Craig-Bampton operator of Equation (5) with fixed-interface modes restricted to the retained ones, and

$$\mathbf{u}_{\mathrm{rec}} = \begin{bmatrix} \mathbf{u}_{\mathrm{i,rec}} \\ \mathbf{u}_{\mathrm{b}} \end{bmatrix}, \tag{41}$$

with the displacements

$$\mathbf{u}_{\mathrm{i,rec}} \approx \boldsymbol{\Phi}_{\mathrm{r}}\boldsymbol{\eta}_{\mathrm{r}} + \boldsymbol{\Psi}\mathbf{u}_{\mathrm{b}} + \boldsymbol{\Phi}_{\mathrm{s}}\boldsymbol{\eta}_{\mathrm{s}}^{(1)} + \boldsymbol{\Phi}_{\mathrm{c}}\boldsymbol{\mathcal{X}}_{\mathrm{c}}(\boldsymbol{\eta}_{\mathrm{r}}, \dot{\boldsymbol{\eta}}_{\mathrm{r}}). \tag{42}$$

Here, the third term represents the first-order slave response reconstructed through residual flexibility, which reads:

$$\boldsymbol{\Phi}_{\mathrm{s}}\boldsymbol{\eta}_{\mathrm{s}}^{(1)} \approx \omega^2\left(\mathbf{F}_{\mathrm{res}} + \omega^2\mathbf{F}_{\mathrm{res}}\mathbf{M}_{\mathrm{ii}}\mathbf{F}_{\mathrm{res}}\right)\mathbf{W}\mathbf{u}_{\mathrm{b}}, \tag{43}$$

while the last term of Equation (42) approximates the third-order slave contribution.

Moreover, the third-order contribution associated with slave inertial terms is:

$$\overline{\mathbf{f}}_{\mathrm{in}}^{(3)}(\boldsymbol{\eta}_{\mathrm{r}},\dot{\boldsymbol{\eta}}_{\mathrm{r}}) = \begin{bmatrix} \mathbf{0} \\ \widehat{\mathbf{M}}_{\mathrm{bs}} \dfrac{\mathrm{d}^2}{\mathrm{d}t^2}\boldsymbol{\mathcal{X}}(\boldsymbol{\eta}_{\mathrm{r}},\dot{\boldsymbol{\eta}}_{\mathrm{r}}) \end{bmatrix}. \tag{44}$$

The nonlinear forces in Equations (40) and (44) depend only on the retained and boundary coordinates. Instead of solving the resulting nonlinear reduced equations, these forces are evaluated along a harmonic motion prescribed by the linear Bloch mode of Equation (38). For a selected Bloch mode, a harmonic ansatz is introduced as

$$\widetilde{\mathbf{u}}(q,A,t) = A\left(\Re(\overline{\mathbf{B}}_q\boldsymbol{\varphi})\cos\omega t + \Im(\overline{\mathbf{B}}_q\boldsymbol{\varphi})\sin\omega t\right), \tag{45}$$

where $\overline{\mathbf{B}}_q\boldsymbol{\varphi}$ is the lifted Bloch eigenvector and $\omega = \omega_n(q)$. The eigenvector is assumed to be mass-normalized, $\boldsymbol{\varphi}^{\mathsf{H}}\overline{\mathbf{M}}_{\mathrm{e},q}\boldsymbol{\varphi} = 1$, so A can be interpreted as a Bloch modal amplitude.

Let $\widetilde{\mathbf{u}}_{\mathrm{r}}(t)$ and $\widetilde{\mathbf{u}}_{\mathrm{b}}(t)$ denote the retained modal and boundary blocks of Equation (45). Evaluating the forces of Equations (40) and (44) along this orbit gives

$$\begin{aligned} \widetilde{\mathbf{r}}(t) &= \widetilde{\mathbf{g}}(t) + \widetilde{\mathbf{f}}_{\mathrm{in}}^{(3)}(t), \\ \widetilde{\mathbf{g}}(t) &= \overline{\mathbf{g}}\big(\widetilde{\mathbf{u}}_{\mathrm{r}}(t),\, \dot{\widetilde{\mathbf{u}}}_{\mathrm{r}}(t),\, \widetilde{\mathbf{u}}_{\mathrm{b}}(t)\big), \\ \widetilde{\mathbf{f}}_{\mathrm{in}}^{(3)}(t) &= \overline{\mathbf{f}}_{\mathrm{in}}^{(3)}\big(\widetilde{\mathbf{u}}_{\mathrm{r}}(t),\, \dot{\widetilde{\mathbf{u}}}_{\mathrm{r}}(t)\big). \end{aligned} \tag{46}$$

The corrected frequency $\widetilde{\omega}(q,A)$ is then obtained in two steps. First, the force $\widetilde{\mathbf{r}}$ is sampled along the orbit over one linear period $T = 2\pi/\omega$, projected onto the independent Bloch coordinates, and reduced to its complex fundamental amplitude,

$$\widetilde{\mathbf{r}}_1 = \frac{2}{T}\int_0^T \overline{\mathbf{B}}_q^{\mathsf{H}}\,\widetilde{\mathbf{r}}(t)\,e^{\mathrm{j}\omega t}\,\mathrm{d}t, \tag{47}$$

which is the component of the projected force synchronous with the reference motion. Higher harmonics are orthogonal to $e^{\mathrm{j}\omega t}$ over one period and do not contribute. Second, $\widetilde{\mathbf{r}}_1$ is projected onto the linear Bloch mode, which gives the amplitude-dependent frequency in Rayleigh-quotient form

$$\widetilde{\omega}^2(q,A) = \omega^2(q) + \frac{\Re\big(\boldsymbol{\varphi}^{\mathsf{H}}\widetilde{\mathbf{r}}_1\big)}{A\,\boldsymbol{\varphi}^{\mathsf{H}}\overline{\mathbf{M}}_{\mathrm{e},q}\boldsymbol{\varphi}}. \tag{48}$$

The imaginary part of $\boldsymbol{\varphi}^{\mathsf{H}}\widetilde{\mathbf{r}}_1$ is proportional to the work done by $\widetilde{\mathbf{r}}$ over one period, which vanishes for the conservative system considered here. Since the reconstruction does not preserve this property exactly, retaining only the real part enforces the zero-work condition and discards a small spurious contribution.

Notably, the amplitude A scales the complete Bloch orbit. Along this orbit, each master coordinate oscillates with amplitude $A_m = A|\varphi_m|$, where φ_m is the corresponding entry of $\boldsymbol{\varphi}$. This is the characteristic amplitude used in Section 2.3. The

mappings are parametrized by the radius ρ of Equation (24). Since the master oscillates at the Bloch frequency ω rather than at ω_m, its state describes an ellipse in the plane $(\eta_m, \dot{\eta}_m/\omega_m)$, with instantaneous radius

$$\rho_m(q, A, t) = \sqrt{\eta_m^2(t) + \frac{\dot{\eta}_m^2(t)}{\omega_m^2}}, \tag{49}$$

which varies between A_m and $A_m\,\omega/\omega_m$. The fitting radius $\rho_{m,\max}$ of Section 2.3 must thus exceed the maximum of Equation (49) over the wavenumbers and amplitudes at which the mappings are evaluated.

3 Note on computational complexity

In the proposed formulation, the reference orbit is prescribed by the linear Bloch eigenvector, and the frequency estimate follows from force sampling over one period, without nonlinear iterations at each (q, A). Conventional harmonic balance, on the other hand, determines the frequency and the Fourier coefficients of the response simultaneously [14]. The two approaches are compared below in terms of recurring operations, for a grid of N_q wavenumbers, N_A amplitudes, and N_n branches.

The proposed method consists of a preliminary and an evaluation stage, as detailed in Section 2. The preliminary stage computes the quantities shared by all points of the dispersion curves once, and requires: (i) computing $N_\mathrm{r} + N_\mathrm{c}$ eigensolutions of the fixed-interface eigenproblem of size N_i (which can be solved with iterative eigensolvers to avoid the complete eigendecomposition), (ii) computing the constraint modes and the residual-flexibility operators, and (iii) performing the fixed-point iterations that determine the single-master mappings.

In the evaluation stage, for each wavenumber, the residual-enhanced Bloch eigenproblem of Equation (38) is assembled and solved, providing the eigenvectors used to define the harmonic orbits of all considered branches and amplitudes. For each orbit, the nonlinear correction requires the reconstruction of the slave coordinates and physical displacements (Equation (42)), followed by the calculation and projection of the nonlinear forces at N_t samples over one period. The total cost in the evaluation stage is thus

$$\mathcal{C}_\mathrm{ROM} = N_q\,\mathcal{C}_\mathrm{CB}(N_\mathrm{ROM}) + N_q N_A N_n N_\mathrm{t}\,\mathcal{C}_\mathrm{sample}, \tag{50}$$

where $\mathcal{C}_\mathrm{CB}(N_\mathrm{ROM})$ denotes the cost of assembling and solving the residual-enhanced Bloch eigenproblem (with $N_\mathrm{ROM} = N_\mathrm{r} + N_\mathrm{L}$), and $\mathcal{C}_\mathrm{sample}$ is the cost of reconstructing the response and calculating the nonlinear correction at one orbit sample.

For comparison, a one-term harmonic balance of the full-order cell (Appendix A) requires N_it iterations for each branch, wavenumber, and amplitude, with an update of the nonlinear stiffness and the solution of an eigenproblem at each iteration. Its cost is

$$\mathcal{C}_\mathrm{HB} = N_q N_A N_n N_\mathrm{it}\left[\mathcal{C}_\mathrm{eig}(N_\mathrm{FOM}) + \mathcal{C}_\mathrm{update}\right], \tag{51}$$

where $\mathcal{C}_\mathrm{eig}(N_\mathrm{FOM})$ is the cost of the full-order eigenproblem (with $N_\mathrm{FOM} = N - N_\mathrm{L}$) and $\mathcal{C}_\mathrm{update}$ accounts for the nonlinear stiffness update, including force sampling.

For dense eigensolvers, $\mathcal{C}_{\text{eig}}(N_{\text{FOM}}) = \mathcal{O}(N_{\text{FOM}}^3)$ and $\mathcal{C}_{\text{CB}}(N_{\text{ROM}}) = \mathcal{O}(N_{\text{ROM}}^3)$. Moreover, the cost of each nonlinear evaluation in the proposed method can be estimated as

$$\mathcal{C}_{\text{sample}} = \mathcal{O}\left(N_{\text{r}}N_{\text{c}}(p+1) + N_{\text{i}}(N_{\text{r}} + N_{\text{c}} + N_{\text{b}})\right), \tag{52}$$

where the first term accounts for the single-master mappings and the second for displacement reconstruction and force evaluation and projection, assuming local nonlinearities. Here, N_{i} represents an upper bound, since only the DOFs involved in nonlinear elements need to be reconstructed. Similarly, for local nonlinearities, $\mathcal{C}_{\text{update}}$ includes a force-sampling cost of order $\mathcal{O}(N_{\text{t}}N_{\text{i}})$, in addition to any stiffness-assembly operations.

Notably, unlike harmonic balance, the proposed method does not require repeated eigenproblems or nonlinear iterations at each amplitude, since the linear Bloch eigenvectors are reused throughout the nonlinear correction.

For large cells, assuming that $N_{\text{FOM}} \approx N_{\text{i}}$, the ratio between the two computational costs is:

$$\begin{aligned}
\frac{\mathcal{C}_{\text{HB}}}{\mathcal{C}_{\text{ROM}}} &= \frac{N_A N_n N_{\text{it}} \left[\mathcal{C}_{\text{eig}}(N_{\text{FOM}}) + \mathcal{C}_{\text{update}}\right]}{\mathcal{C}_{\text{CB}}(N_{\text{ROM}}) + N_A N_n N_{\text{t}}\, \mathcal{C}_{\text{sample}}} \\
&\approx \frac{N_{\text{it}}\mathcal{C}_{\text{eig}}(N_{\text{i}})}{N_{\text{t}}\, \mathcal{C}_{\text{sample}}} \\
&\sim \frac{\mathcal{O}(N_{\text{i}}^3)}{\mathcal{O}(N_{\text{i}})} = \mathcal{O}(N_{\text{i}}^2)
\end{aligned} \tag{53}$$

since $\mathcal{C}_{\text{HB}}$ is dominated by its eigenproblem term, whereas, for fixed N_{r} and N_{c}, $\mathcal{C}_{\text{ROM}}$ is dominated by the force sampling, which grows only linearly with N_{i}. Notably, this ratio grows as N_{i}^2 for dense eigensolvers.

4 Criteria for mode selection

The reduced model proposed in this work mainly depends on three choices: the fitting radius $\rho_{m,\max}$ of the mappings, the set $\mathcal{R}$ of retained fixed-interface modes, and, for large models, the subset $\mathcal{S}_{\text{c}}$ of slave modes for which the mappings are computed (see Section 2.3). While the fitting radius follows from the amplitudes of interest discussed in Section 2.5, the selection of $\mathcal{R}$ and $\mathcal{S}_{\text{c}}$ is addressed herein.

A first requirement pertains to the pure linear response: the retained set $\mathcal{R}$ must be sufficiently rich for the reduced Bloch problem to accurately reproduce the full-order eigenpair on the branch and at the wavenumber of interest. A classical modal-truncation guideline from CMS suggests retaining fixed-interface modes up to a cutoff frequency sufficiently above the Bloch frequency of interest, commonly by a factor of 1.5 to 2 [4]. When the dispersion relation is required at specific wavenumbers, a more accurate criterion can be used, since the number of required modes generally varies along a branch. The criterion proposed in Appendix B assesses the retained set through the error in the reduced Bloch eigenvectors.

In the nonlinear case, the retained set $\mathcal{R}$ must also allow the slave reconstruction to be computed. Once a retained set has been chosen, it must thus be checked for internal resonances with the reconstructed slave modes in $\mathcal{S}_{\text{c}}$. These occur when a slave

frequency approaches a harmonic generated by a retained master, which may render the manifold reconstruction ill-conditioned. At exact resonance, the slave coordinate cannot be represented as a smooth, uniquely slaved function of the master pair.

For an odd nonlinearity of degree p, a single-master motion generates harmonics $k = 1, 3, \ldots, p$ of the master frequency, and the linearized slave operators contain the factors $\omega_s^2 - k^2\omega_m^2$.

For every retained master in $\mathcal{R}$ and computed slave mode in $\mathcal{S}_c$, proximity to these ratios can be described and controlled by the dimensionless detuning index

$$\alpha_s = \frac{\omega_s^2}{\min\limits_{m\in\mathcal{R},\ k\in\{1,3,\ldots,p\}} \left|\omega_s^2 - k^2\omega_m^2\right|} < \alpha_{\max}. \tag{54}$$

Every slave whose α_s exceeds a user-defined threshold $\alpha_{\max}$ must be promoted to the retained set $\mathcal{R}$. The screening can also be repeated until no remaining slave violates the threshold. For $\omega_s > p\,\omega_{\max}$, where $\omega_{\max}$ is the highest frequency in the retained set $\mathcal{R}$, $\alpha_s = \omega_s^2/(\omega_s^2 - p^2\omega_{\max}^2)$ decreases with ω_s and falls below $\alpha_{\max}$ for all $\omega_s \geq \omega_{\text{cut}}$ with

$$\omega_{\text{cut}} = p\,\omega_{\max}\sqrt{\alpha_{\max}/(\alpha_{\max} - 1)}. \tag{55}$$

Therefore, when the mappings are computed only for a subset of the slave modes $\mathcal{S}_c$, this subset must include all slave modes below ω_{cut} (e.g., $\omega_{\text{cut}} \approx 3.2\,\omega_{\max}$ for $p = 3$ and $\alpha_{\max} = 10$).

5 Numerical results

The proposed methodology is demonstrated considering a one-dimensional periodic waveguide consisting of locally resonant unit cells comprising a host chain and a nonlinear resonator chain. In the unit cell, the host has 2 cell-interface half-masses and 7 interior masses m_{h}, connected by 8 linear springs k_{h}. The resonator consists of 7 masses connected in series by 8 springs with alternating linear coefficients k_{r1} and k_{r2} and a common cubic coefficient κ_{r}. The cell has $N = 16$ DOFs: 9 host coordinates, including the 2 boundaries, and 7 resonator coordinates. Hence $N_{\text{i}} = 14$ and $N_{\text{L}} = N_{\text{R}} = 1$. Figure 1 shows a schematic of the unit cell, and Table 1 lists the parameter values in consistent non-dimensional units.

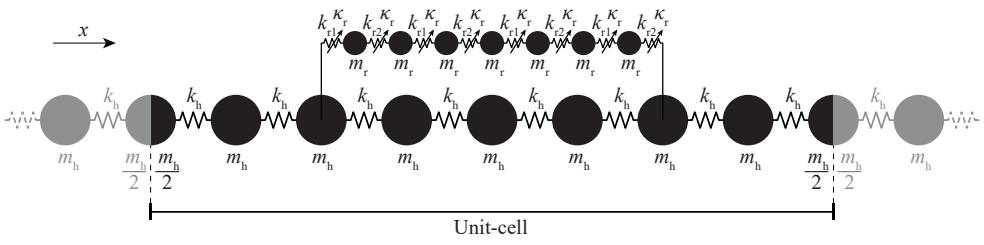

Fig. 1 Locally resonant unit cell used in the numerical benchmark.

Table 1 Parameters of the unit cell. Shared interface half-masses assemble into one host mass.

Parameter	Symbol	Value
Host mass	m_{h}	10
Resonator mass	m_{r}	5
Host spring	k_{h}	8000
Linear resonator springs (alternating)	$k_{\mathrm{r}1}, k_{\mathrm{r}2}$	300, 200
Resonator cubic coefficient	κ_{r}	1500
Cell length	a	1

Since the parameters of Table 1 are expressed in units of a reference mass m^*, stiffness k^* and length a, times are measured in units of $\tau = \sqrt{m^*/k^*}$. Frequencies are normalized by the upper edge of the linear acoustic branch, $\omega_0 \approx 2.66/\tau$.

5.1 Mode selection and dispersion relation

The retained set is selected with the procedure described in Section 4 and Appendix B, applied to the first three Bloch branches over $q \in [0, \pi/a]$. First, for each branch and wavenumber, the linear criterion of Appendix B is used to determine the smallest number of baseline modes N_{r} to reproduce the full-order Bloch eigenvector with a MAC threshold of $1 - \varepsilon = 0.99$, as shown in Figure 2(a). Since the model is small, the untruncated eigenpairs are used as reference. The figure shows that branch 1 requires a single mode over the whole interval. Branches 2 and 3 require few modes away from their central intervals: one or two for branch 2, and two or three for branch 3. Around their central intervals, the basis must be extended to $N_{\mathrm{r}} = 5$. Consistently with Appendix B, these intervals lie around the maximum group velocity of the respective branches.

Given this baseline order, Figure 2(b) shows the number N_{r}^{+} of additional modes promoted by the condition $\alpha_s > \alpha_{\max} = 10$. The screening depends on the fixed-interface frequencies and on the current retained set: its apparent dependence on branch and wavenumber is indirect, through the baseline value of N_{r}.

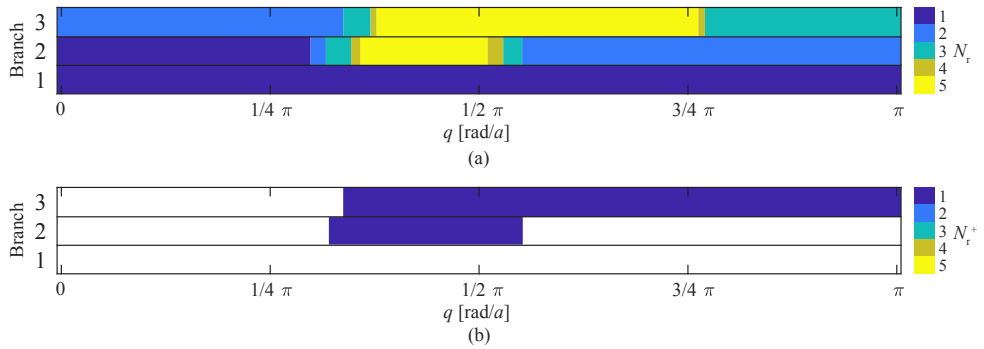

Fig. 2 Model order: (a) smallest number of retained modes satisfying the MAC threshold, (b) number of promoted slave modes.

Based on Figure 2, the first five fixed-interface modes are chosen to form the baseline retained set. Moreover, mode 9 is promoted because of its near $3:1$ ratio with master mode 3 ($\omega_9/\omega_3 \approx 2.94$, $\alpha_9 \approx 24$). After this promotion, $\omega_{\text{cut}} \approx 26.1\omega_0$ exceeds the highest fixed-interface frequency, so the mappings are computed for all 8 slave modes.

Figure 3 illustrates four of the single-master slave-reconstruction functions. Since the basis of Equation (26) is homogeneous, all functions scale as ρ^3, and their dependence on the polar angle θ contains only the first and third harmonics. For master 1 ($\omega_6/\omega_1 = 4.57$ and $\omega_7/\omega_1 = 4.92$), the slave frequencies lie well above $3\omega_1$, and the third harmonic is in phase with the fundamental and about half of it. Thus, the functions follow the master displacement, with extrema at $\theta = 0$ and π, and become nearly flat around $\theta = \pi/2$ and $3\pi/2$. For master 2 ($\omega_6/\omega_2 = 2.32$ and $\omega_7/\omega_2 = 2.50$), the slave frequencies lie closer to $3\omega_2$, so that the third harmonic becomes comparable to the fundamental and in antiphase with it. The two contributions nearly cancel at $\theta = 0$ and π, where the master displacement is maximum (or minimum), and the functions attain their extrema at intermediate phases. The functions associated with master 2 are also 6 to 30 times larger, owing to stronger modal coupling with slaves 6 and 7. Nevertheless, the reconstructed slave amplitudes remain below about 5% of ρ over the fitting range. The mappings are fitted over $\rho_{m,\max} = 1.5$, which covers the largest radius reached along the Bloch orbits, $\rho \approx 1.43$ for master 1 on branch 2 at $A = 1$.

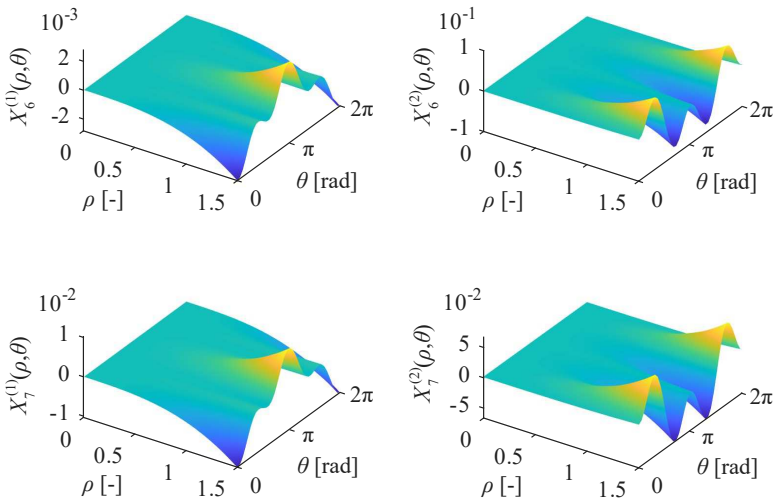

Fig. 3 Single-master slave-reconstruction functions in polar coordinates for master modes 1 and 2 and slave modes 6 and 7.

The final ROM has 8 coordinates: 6 retained modal coordinates and 2 physical boundary coordinates. The dispersion relation is evaluated through Equation (48) for the first three Bloch branches over $q \in [0, \pi/a]$ and $A \in [0.01, 1]$. Figure 4 shows the resulting surfaces, colored from yellow at $A = 0.01$ to magenta at $A = 1$. All three branches recover the linear result as $A \to 0$ and exhibit a hardening shift over the investigated range.

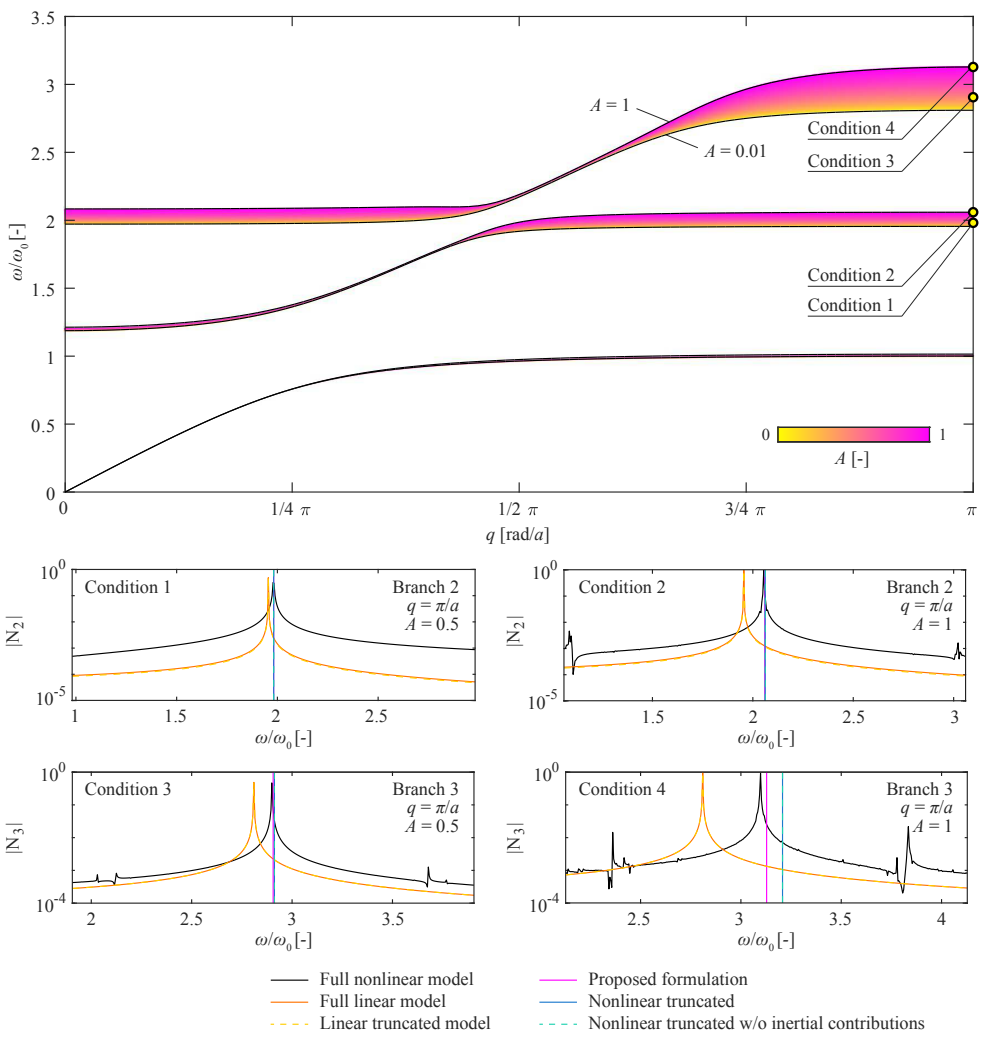

Fig. 4 Amplitude-dependent dispersion surfaces obtained with 5 baseline master modes and 1 promoted mode (top), and response spectra of the fixed-interface modal coordinates η_2 and η_3 for the four test conditions at $q = \pi/a$ (bottom). Frequencies are normalized by ω_0, the upper edge of the linear acoustic branch.

In the bottom part, Figure 4 also reports the response spectra for four test conditions at the boundary of the first Brillouin zone ($q = \pi/a$), marked on the dispersion surfaces: branch 2 with $A = 0.5$ (condition 1) and $A = 1$ (condition 2), and branch 3 with $A = 0.5$ (condition 3) and $A = 1$ (condition 4). Each spectrum is computed from the free-vibration response obtained by directly integrating the full nonlinear equations of the unit cell in Figure 1, subject to the corresponding Bloch boundary

conditions and the initial conditions

$$\mathbf{u}(0) = A\boldsymbol{\varphi}^{\mathrm{phys}}_{\mathrm{full},n}, \qquad \dot{\mathbf{u}}(0) = \mathbf{0}, \tag{56}$$

where

$$\boldsymbol{\varphi}^{\mathrm{phys}}_{\mathrm{full},n} = \mathbf{T}\mathbf{B}_q\boldsymbol{\varphi}_{\mathrm{full},n}, \tag{57}$$

and $\boldsymbol{\varphi}_{\mathrm{full},n}$ is the n-th mass-normalized eigenvector of the full linear Bloch problem, while $\mathbf{B}_q$ is the full-order Bloch operator. At $q = \pi/a$, the Bloch conditions reduce to $\mathbf{u}^{\mathrm{R}}_{\mathrm{b}} = -\mathbf{u}^{\mathrm{L}}_{\mathrm{b}}$, so that the eigenvector is real and the response of a single cell can be integrated directly. The plots report the Fourier amplitudes of the fixed-interface modal coordinates η_2 and η_3 for branches 2 and 3, respectively ($|N_2| = |\mathcal{F}(\eta_2)|$ and $|N_3| = |\mathcal{F}(\eta_3)|$). At $q = \pi/a$, these coordinates dominate the corresponding Bloch eigenvectors, whose boundary participation is small, so that the spectra coincide with those of the Bloch modal coordinates.

The plots also include the spectra of the full linear model (obtained by setting $\mathbf{g}(\mathbf{u}) = \mathbf{0}$) and of the linear truncated model (constructed with the same fixed-interface modes retained in the proposed formulation). The two linear spectra almost coincide, which supports the adequacy of the retained modal basis. The full nonlinear model exhibits a clear hardening behavior, with the main peak shifting above the linear one as the amplitude increases (by up to 10% of the linear frequency in condition 4).

The vertical lines mark the frequencies predicted by Equation (48) at the same (q, A) for three variants: the full proposed formulation, which includes the promoted mode, the slave reconstruction, and the inertial contributions ($\bar{\mathbf{f}}_{\mathrm{in}}$); a nonlinear truncated model, which uses only the N_{r} baseline modes, without promotion and slave reconstruction; and the same truncated model without the inertial contributions. The full proposed formulation is generally the closest to the nonlinear peak. For moderate nonlinear activation (conditions 1-3), the three predictions are close to each other, and the frequency shift is largely captured by the retained coordinates alone. At the largest amplitude on branch 3 (condition 4), the truncated predictions overestimate the nonlinear peak frequency by 3.5%, i.e., by about one third of the nonlinear shift, whereas the proposed formulation reduces the error to 1%. Thus, the promoted mode and the slave reconstruction become relevant as the nonlinear activation grows. The residual overestimation of the proposed formulation is consistent with the prescribed reference orbit, which does not adapt the mode shape to the amplitude.

In contrast, the predictions with and without the inertial contributions are indistinguishable in all conditions. At a fixed wavenumber, these terms shift the frequency by an amount of the order of the linear truncation error, which is small here. Their effect becomes relevant when the wavenumber is evaluated at a prescribed frequency, where it is amplified by the inverse of the group velocity, as shown in Section 6.3.

5.2 Mode participation and nonlinear activation

The dominant-master assumption of Section 2.3 is assessed here by calculating the participation of each fixed-interface coordinate $\eta^{(n)}_m(q)$ in the Craig-Bampton representation of the full linear Bloch eigenvector $\boldsymbol{\varphi}_{\mathrm{full},n}$. For mass-normalized fixed-interface

modes, the relative participation factors are

$$\gamma_m^{(n)}(q) = \frac{|\eta_m^{(n)}(q)|^2}{\sum_{l=1}^{N_\mathrm{i}} |\eta_l^{(n)}(q)|^2}. \tag{58}$$

Figure 5 shows that fixed-interface mode 1 dominates branch 1 and the first part of branch 2, mode 2 dominates the last part of branch 2 and the first part of branch 3, and mode 3 dominates the last part of branch 3. Although the dominant mode changes with the wavenumber, a single mode generally dominates, except in the transition regions. This supports the dominant-master assumption over much of the investigated range, where the sum of all contributions collapses into the effects of a single dominant mode. In the transition regions, where the master mode contributions become comparable, the sum in Equation (27) remains a valid approximation provided that the nonlinearity is small.

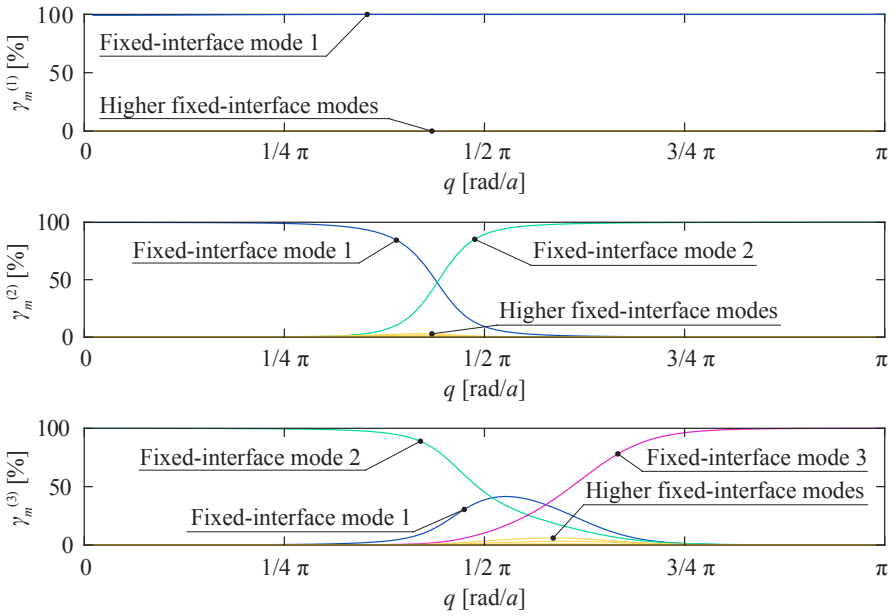

Fig. 5 Relative fixed-interface modal weights for the first three full-order Bloch branches.

This is also visible in Figure 4, where the branches change only slightly with amplitude in the regions of higher group velocity. The weak nonlinear activation in these regions is confirmed by Figure 6, which reports, at $A = 1$, the ratio μ_n between the nonlinear and linear restoring-force contributions at the fundamental harmonic. This ratio is obtained by projecting the linear and nonlinear forces of the full-order cell onto the corresponding Bloch mode (see Appendix C). The intervals in which several fixed-interface modes participate appreciably have comparatively small μ_n,

particularly on branches 2 and 3. Thus, where the dominant-master assumption is least accurate, the nonlinear correction is also weakest relative to the linear contribution.

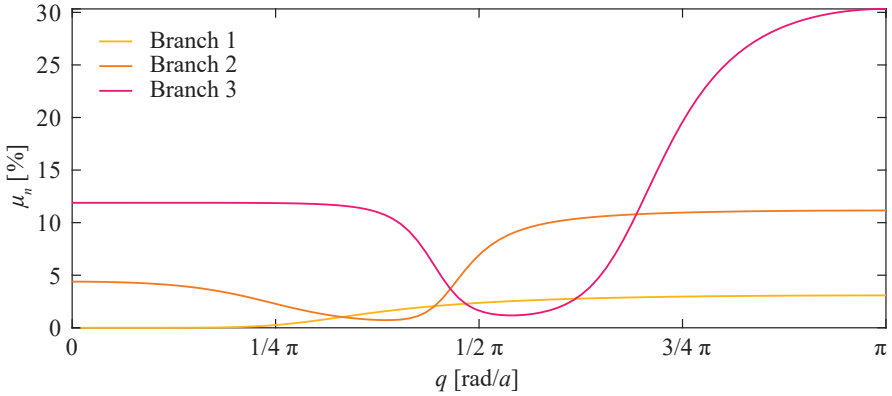

Fig. 6 Ratio between nonlinear and linear spring-force contributions at the fundamental harmonic for the first three Bloch branches at $A = 1$.

6 Finite-element validation

The amplitude-dependent dispersion relation obtained with the proposed method is validated against time-domain simulations of a finite chain of resonating cells, modeled in COMSOL Multiphysics [34]. A narrow-band, smoothly ramped harmonic displacement is imposed at one end of the chain, and the wave transmitted into the chain is analyzed at the excitation frequency to estimate the effective wavenumber and the corresponding modal amplitude for different physical input amplitudes.

6.1 Model description

The FE model is built with the Truss interface of the Structural Mechanics Module, in a two-dimensional geometry, and consists of 600 repetitions of the unit cell described in Section 5. All springs are modeled as single linear truss elements with spring-damper constitutive laws. The host springs have linear stiffness k_{h}, whereas the resonator springs follow

$$f_e = k_e \Delta u_e + \kappa_e \Delta u_e^3, \tag{59}$$

where Δu_e is the elongation of spring e. In the resonant spring chain, stiffnesses alternate between k_{r1} and k_{r2}, while the cubic coefficient is κ_{r} for all springs. Geometric nonlinearity is disabled.

The masses are introduced as point masses, m_{r} at the resonator nodes and m_{h} at the host nodes, including the boundary nodes shared by neighboring cells, which carry the two half-masses of the adjacent cells.

The transverse displacements are constrained. Therefore, the motion is purely axial, and the FE model is equivalent to the discrete model of Section 5. No viscous or structural damping is assigned, and the right end of the chain is clamped.

The first host node (left boundary of cell 1) is driven by a smoothly ramped tone, imposed as a prescribed displacement:

$$u(t) = u_{\mathrm{I}}\, w(t) \sin(\omega_{\mathrm{I}} t), \tag{60}$$

where

$$w(t) = \beta^3(10 - 15\beta + 6\beta^2), \qquad \beta = \min(t/T_{\mathrm{ramp}}, 1), \quad t \geq 0, \tag{61}$$

with $T_{\mathrm{I}} = 2\pi/\omega_{\mathrm{I}}$ and $T_{\mathrm{ramp}} = 40T_{\mathrm{I}}$. The ramp has continuous first and second derivatives, which limits the spectral content of the input to a narrow band around ω_{I}.

Branches 2 and 3 are tested in two separate sets of analyses, with $\omega_{\mathrm{I}} = 1.95\omega_0$ and $\omega_{\mathrm{I}} = 2.78\omega_0$, respectively. In the linear limit, these frequencies correspond to $q \approx 0.619\pi/a$ and $q \approx 0.815\pi/a$, respectively. Both points lie on the upper portion of the relevant branch, where the group velocity is small ($c_{\mathrm{g}} \approx 0.07a/\tau$ and $0.30a/\tau$, respectively, compared with maxima of about $2.4a/\tau$ and $2.6a/\tau$) and the wavenumber is highly sensitive to the amplitude-dependent frequency shift. Independent analyses are conducted with prescribed amplitudes $u_{\mathrm{I}} = 0.01a$, $0.02a$, $0.03a$, and $0.04a$.

The equations of motion are integrated with the generalized-α method, with spectral radius at infinite frequency $\rho_\infty = 0.75$, which controls the algorithmic dissipation of the high-frequency components. A fixed time step $\Delta t = (2\pi/\omega_{\mathrm{I}})/200$ is used (i.e., 200 steps per excitation period). The nonlinear system is solved at each step by a fully coupled Newton-Raphson scheme, and the solution is stored at every time step. The algorithmic dissipation of the scheme acts on the high-frequency content and is the only source of dissipation in the model.

6.2 Estimation of wavenumber and modal amplitude

The displacement histories of all nodes of cells 3 to 12 are post-processed in a time window in which the transient front has passed. This spatial interval excludes the cells closest to the excitation, and it is short enough for the amplitude of the propagating wave to be nearly uniform across the analyzed cells.

In this window, the amplitude U_j at ω_{I} of each DOF is obtained by a least-squares fit of

$$u_j(t) \approx \Re\big(U_j\, e^{-\mathrm{j}\omega_{\mathrm{I}} t}\big). \tag{62}$$

The fit suppresses content at frequencies other than ω_{I}, including the third harmonic generated by the cubic springs.

From the fitted complex amplitudes U_j, the amplitudes U_c^{b} of the right boundary DOFs of the ten cells are extracted. Their spatial Fourier transform provides an estimate of the wavenumber q.

To estimate the Bloch modal amplitude A, the amplitudes U_j of the N DOFs of each cell c are collected in the vector $\mathbf{U}_c$ and projected onto the mass-normalized Bloch mode of Equation (57), evaluated for the considered branch at the estimated wavenumber. This gives $A_c = \big|\boldsymbol{\varphi}_{\mathrm{full},n}^{\mathrm{phys}\,\mathsf{H}}\, \mathbf{M}\mathbf{U}_c\big|$, which is averaged over the ten cells to reduce the sensitivity to local deviations.

Figure 7 shows the input and the response at cells 3, 15, and 30 for $u_{\mathrm{I}} = 0.01a$ and $\omega_{\mathrm{I}} = 2.78\omega_0$. The input ramp ends at $t \approx 48.5\tau$ on branch 2 and $t \approx 33.9\tau$ on branch 3,

and the wavefront crosses the analyzed cells within about 220τ and 70τ, respectively. To exclude this transient, the signals are analyzed in the windows $300\tau \leq t \leq 400\tau$ for branch 2 and $200\tau \leq t \leq 300\tau$ for branch 3. A slow modulation of the envelope persists in these windows, due to components at frequencies close to ω_{I} excited during the ramp. Since each window spans a few modulation periods, these components are suppressed by the least-squares fit, which retains only the response at ω_{I}.

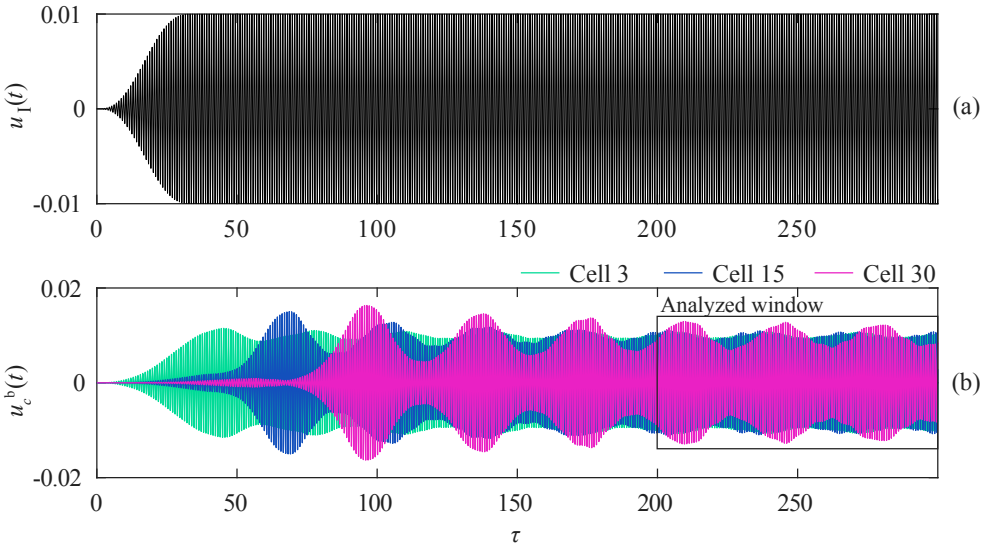

Fig. 7 Time histories of the FE chain for branch 3 ($\omega_{\mathrm{I}} = 2.78\omega_0$, $u_{\mathrm{I}} = 0.01a$): (a) displacement imposed at the first host DOF; (b) displacement of the right boundary DOF of cells 3, 15, and 30. The highlighted area marks the time window used to estimate q and A.

6.3 Comparison with the amplitude-dependent dispersion curves

Figure 8 compares the wavenumbers identified through the FE simulations with the amplitude-dependent dispersion curves obtained with the proposed method. For each input amplitude, the ROM branch is evaluated at the modal amplitude measured in the chain. As u_{I} increases from $0.01a$ to $0.04a$, the modal amplitude grows from $A \approx 0.32$ to 0.73 on branch 2 and from $A \approx 0.27$ to 0.66 on branch 3, and the wavenumber at ω_{I} decreases, consistently with the hardening shift of the branches. On branch 2, q moves from $0.552\pi/a$ to $0.495\pi/a$, i.e., 11% to 20% below the linear value $0.619\pi/a$, although the corresponding frequency shift at fixed q (the linear one) is about 2.7% for the maximum amplitude value. On branch 3, q decreases from $0.768\pi/a$ to $0.712\pi/a$, i.e., 6% to 13% below the linear value $0.815\pi/a$, for frequency shifts of at most 4.9% at the linear wavenumber for the maximum amplitude value. These results illustrate the amplification of small frequency shifts into large wavenumber shifts on the flat

portions of the branches. In all cases, the FE wavenumber lies close to the intersection of the ROM branch with $\omega = \omega_{\mathrm{I}}$.

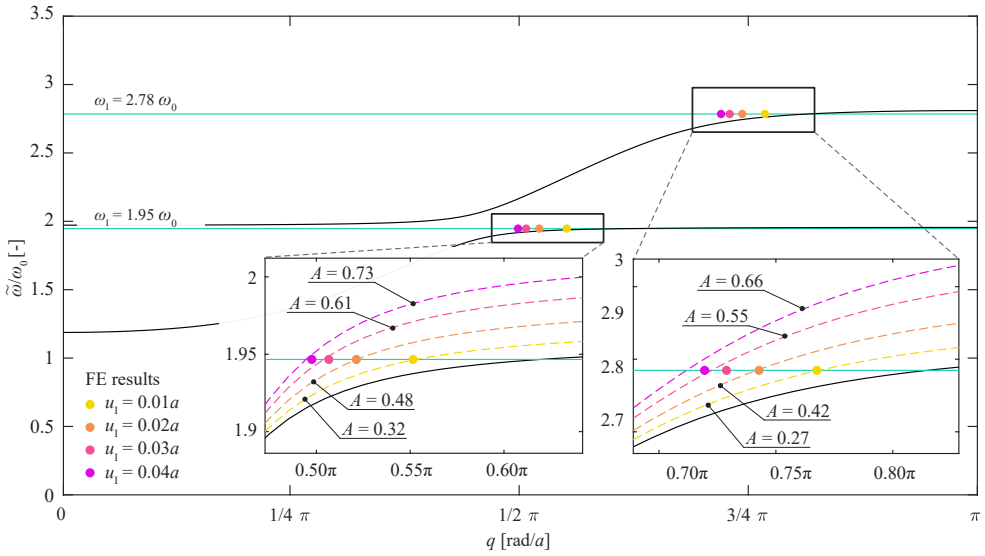

Fig. 8 FE results in the dispersion plane for branch 2 ($\omega_{\mathrm{I}} = 1.95\omega_0$) and branch 3 ($\omega_{\mathrm{I}} = 2.78\omega_0$): ROM branches at $A = 0.01$ (black), ROM branches at the modal amplitude measured for each input amplitude (dashed colored), and FE wavenumber at $\omega = \omega_{\mathrm{I}}$ (colored points).

To investigate the amplitude dependence of these differences, Figure 9 reports the wavenumber at ω_{I} as a function of the modal amplitude. The ROM curve is obtained from the dispersion surfaces of Figure 4 by solving $\tilde{\omega}(q, A) = \omega_{\mathrm{I}}$ for each amplitude. As an additional check, the figure includes a reference solution obtained by one-term harmonic balance (HB) of the full-order unit cell under Bloch conditions, computed as described in Appendix A. Unlike the proposed procedure, the HB solution involves no modal truncation and updates the shape of the Bloch mode with the amplitude. Nevertheless, like the ROM, it neglects higher harmonics.

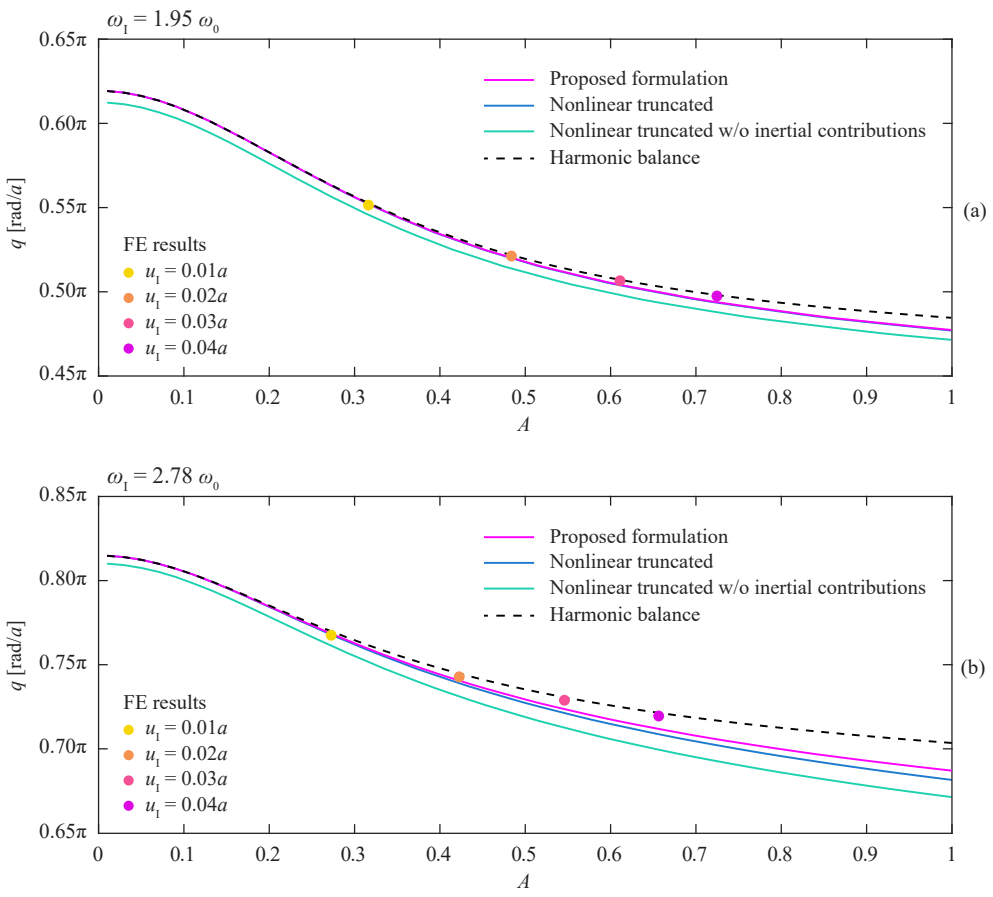

Fig. 9 Wavenumber at the excitation frequency as a function of the modal amplitude for (a) branch 2 and (b) branch 3: proposed formulation, nonlinear truncated model with and without inertial contributions, HB reference, and FE results for $u_\mathrm{I} = 0.01a$, $0.02a$, $0.03a$, and $0.04a$.

The FE results lie close to the HB reference on both branches. At low input amplitude, the proposed formulation also nearly coincides with the FE results. As the amplitude increases, the proposed formulation increasingly underestimates the wavenumber, which corresponds to an overestimated hardening shift. At the largest simulated amplitude ($u_\mathrm{I} = 0.04a$), the difference reaches about $0.003\pi/a$ on branch 2 and $0.008\pi/a$ on branch 3, i.e., about 3% and 8% of the wavenumber shift from the linear value. This trend is consistent with the prescribed reference orbit of Section 2.5, which does not adapt the mode shape to the amplitude, and with the residual overestimation observed in Figure 4.

Figure 9 also isolates the role of the individual contributions. Without the inertial contributions, the truncated model is offset already at small amplitudes, by about $-0.007\pi/a$ on branch 2 and $-0.005\pi/a$ on branch 3. This offset is the linear truncation

error amplified by the small group velocity at ω_{I} (see Section 2.2), and the residual-flexibility correction removes it, so that the truncated model with inertial contributions coincides with the proposed formulation as $A \to 0$. As the amplitude grows, the promoted mode and the slave reconstruction become relevant on branch 3, where the truncated model departs from the proposed formulation and further underestimates the wavenumber, whereas on branch 2 the two curves remain close over the whole range.

In terms of the operations listed in Section 3, the HB solution requires on average about 6, 10 and 15 fixed-point iterations per (q, A) on branches 1, 2 and 3 over the range of Figure 4, with a tolerance of $10^{-12}/\tau$ on ω_{HB}. Each iteration involves an eigenproblem of size $N - N_{\mathrm{L}} = 15$, whereas the proposed formulation solves one eigenproblem of size $N_{\mathrm{r}} + N_{\mathrm{L}} = 7$ per wavenumber, shared by all amplitudes and branches. In this small cell, the size reduction is modest, and the saving comes mainly from the prescribed orbit. The size reduction becomes dominant for unit cells with many internal DOFs. With both methods run in the same environment (MATLAB R2025b, Intel Core i7-8700 at 3.2 GHz, 32 GB RAM; median over 100 repetitions), computing the three branches at $A = 1$ on a grid of 100 wavenumbers takes about 89% less time than HB in the online stage.

7 Conclusions

A nonlinear extension of Bloch mode synthesis was presented to estimate the amplitude-dependent frequency of isolated, weakly nonlinear Bloch branches. The unit cell is reduced by a Craig-Bampton transformation in which a set of fixed-interface modes is retained, and the remaining slave coordinates are treated at three levels of approximation (i.e., truncation, inclusion of their first-order response, and reconstruction of their higher-order response through master-slave mappings). The first-order response, driven by the boundary motion, is evaluated by residual flexibility and enters both the residual-enhanced Bloch eigenproblem, through its inertial coupling with the boundary, and the reconstructed state on which the nonlinear force is evaluated. The higher-order response, which accounts for the nonlinear interaction between retained and slave modes, is reconstructed by single-master nonlinear mappings, computed once on the fixed-interface subsystem and therefore independent of the wavenumber, and enters both the nonlinear force and the inertial coupling. The frequency correction follows from the fundamental harmonic of the reconstructed forces along the linear Bloch orbit, projected onto the Bloch mode through a scalar Rayleigh quotient. Nonlinear equations are solved only offline, so the sweep over wavenumber and amplitude requires only one reduced linear eigenproblem per wavenumber, shared by all amplitudes and branches, and force sampling over one period, whereas a full-order harmonic balance requires, at each wavenumber and amplitude, a fixed-point iteration with a full-size eigenproblem per step.

The required basis of fixed-interface modes was shown to be non-uniform along a branch. A criterion was thus proposed to identify the minimum number of modes, which grows with the group velocity. Moreover, a detuning index was applied to identify the slave modes close to the $k{:}1$ ratios with a retained mode, which are promoted to masters.

As a benchmark, a ROM with 6 modal and 2 boundary coordinates of a 16-DOF locally resonant cell predicted the nonlinear peak frequency of branch 3 at the edge of the Brillouin zone within 1% error at the largest amplitude, against 3.5% for the truncated model. The promoted mode and the slave reconstruction become relevant as the nonlinear activation grows. The residual-flexibility terms have a negligible effect at fixed wavenumber. However, they remove a wavenumber offset of up to $0.007\pi/a$ at prescribed frequency on the flat portions of the branches. In finite-chain simulations, frequency shifts below 5% produced wavenumber shifts of up to 20%. The ROM reproduced this trend, with deviations from the FE wavenumbers of at most 3% and 8% of the wavenumber shift on the two analyzed branches.

From the computational point of view, the evaluation stage of the proposed method requires one reduced eigenproblem per wavenumber and, at a given amplitude, force sampling over one period. For fixed retained and reconstructed sets, its cost grows only linearly with the number of internal DOFs. In the present example, it is about 89% lower than that of harmonic balance, and the saving is expected to increase for larger cells. This saving follows from prescribing the reference orbit through the linear Bloch mode, which removes the nonlinear iterations and repeated full-order eigenproblems required by harmonic balance. The price is that the mode shape does not adapt to the amplitude, so that the hardening shift is increasingly overestimated as the amplitude grows. This limitation could be reduced by an amplitude-dependent update of the mode shape, which will be investigated in future developments.

Declarations

Funding. The authors acknowledge the funding received from the Italian Ministry of University and Research (MUR) for the "EXTREME" project (grand agreement 2022EZT2ZE, CUP: J53C24002870006).

Competing interests. The authors have no relevant financial or non-financial interests to disclose.

Data availability. The datasets generated during the current study are available from the corresponding author on reasonable request.

Author contributions. All authors contributed to the study conception and design. Material preparation and analysis were performed by S.Q. The first draft of the manuscript was written by S.Q., and A.P. reviewed previous versions. All authors read and approved the final manuscript.

Appendix A One-term harmonic balance reference

This section describes the full-order reference used in Section 6.3. A one-term harmonic balance with a Bloch-wave ansatz [14] is applied to the physical coordinates of the unit cell. The resulting amplitude-dependent eigenvalue problem has the form of the single-nonlinear-mode formulation [35] and is solved by fixed-point iteration on the mode shape.

Each spring e connects two DOFs i_e and j_e and follows the force law of Equation (59), with $\kappa_e = \kappa_\mathrm{r}$ for the resonator springs and $\kappa_e = 0$ for the host springs. Denoting by $\mathbf{d}_e$ its incidence vector, with entries $+1$ at i_e, -1 at j_e and zero elsewhere, the elongation is $\Delta u_e = \mathbf{d}_e^\mathsf{T}\mathbf{u}$, and Equation (1) for the cell of Section 5 reads

$$\mathbf{M}\ddot{\mathbf{u}} + \mathbf{K}\mathbf{u} + \sum_e \kappa_e \left(\mathbf{d}_e^\mathsf{T}\mathbf{u}\right)^3 \mathbf{d}_e = \mathbf{f}, \tag{A1}$$

where $\mathbf{f}$ contains the interface tractions, which act only on the boundary DOFs. The Bloch conditions of Equation (30) are imposed through the full-order Bloch operator $\mathbf{B}_q \in \mathbb{C}^{N\times(N-N_\mathrm{L})}$ of Equation (57), which has the same structure in the physical coordinates of Equation (2). As in Equation (33), $\mathbf{B}_q^\mathsf{H}\mathbf{f} = \mathbf{0}$, and the Bloch-reduced linear operators are $\mathbf{K}_q = \mathbf{B}_q^\mathsf{H}\mathbf{K}\mathbf{B}_q$ and $\mathbf{M}_q = \mathbf{B}_q^\mathsf{H}\mathbf{M}\mathbf{B}_q$.

Analogously to Equation (45), consider the ansatz

$$\mathbf{u}(t) = A\,\Re\left(\mathbf{B}_q\boldsymbol{\varphi}_\mathrm{HB}\, e^{-\mathrm{j}\omega_\mathrm{HB}t}\right), \qquad \boldsymbol{\varphi}_\mathrm{HB}^\mathsf{H}\mathbf{M}_q\boldsymbol{\varphi}_\mathrm{HB} = 1, \tag{A2}$$

so that A is the modal amplitude used for the ROM and for the FE estimates. With $\Delta\varphi_e = \mathbf{d}_e^\mathsf{T}\mathbf{B}_q\boldsymbol{\varphi}_\mathrm{HB}$, the elongations are $\Delta u_e(t) = A\,\Re\left(\Delta\varphi_e e^{-\mathrm{j}\omega_\mathrm{HB}t}\right)$, and, since $\cos^3 x = \frac{3}{4}\cos x + \frac{1}{4}\cos 3x$, the fundamental component of the cubic force in spring e has complex amplitude $\frac{3}{4}\kappa_e A^3|\Delta\varphi_e|^2\Delta\varphi_e$. Retaining only this component, i.e., projecting Equation (A1) onto the fundamental harmonic over one period [14], dividing by A, and premultiplying by $\mathbf{B}_q^\mathsf{H}$ gives

$$\left[\mathbf{K}_q + \mathbf{B}_q^\mathsf{H}\mathbf{K}_\mathrm{nl}\mathbf{B}_q - \omega_\mathrm{HB}^2\,\mathbf{M}_q\right]\boldsymbol{\varphi}_\mathrm{HB} = \mathbf{0}, \tag{A3}$$

with

$$\mathbf{K}_\mathrm{nl} = \frac{3}{4}A^2\sum_e \kappa_e\,|\Delta\varphi_e|^2\,\mathbf{d}_e\mathbf{d}_e^\mathsf{T}. \tag{A4}$$

Since $\mathbf{K}_\mathrm{nl}$ is real and symmetric, Equation (A3) is a Hermitian eigenvalue problem whose stiffness depends on the amplitude and on the mode shape itself.

For given q, A, and branch n, a fixed-point solution is thus found as follows:

1. Solve $\mathbf{K}_q\boldsymbol{\varphi} = \omega^2\mathbf{M}_q\boldsymbol{\varphi}$ and take the n-th eigenvector, normalized as in Equation (A2), as the initial guess $\boldsymbol{\varphi}_\mathrm{HB}^{(0)}$.
2. At iteration k, evaluate $\mathbf{K}_\mathrm{nl}$ with $\boldsymbol{\varphi}_\mathrm{HB}^{(k)}$ and solve the eigenvalue problem of Equation (A3).
3. Among its eigenvectors $\boldsymbol{\varphi}_j$, retain the one with the largest mass-weighted MAC with respect to the current iterate, $|\boldsymbol{\varphi}_j^\mathsf{H}\mathbf{M}_q\boldsymbol{\varphi}_\mathrm{HB}^{(k)}|^2/(\boldsymbol{\varphi}_j^\mathsf{H}\mathbf{M}_q\boldsymbol{\varphi}_j)$, which keeps track of the branch. Normalize it as in Equation (A2) and denote it $\boldsymbol{\varphi}_\mathrm{HB}^{(k+1)}$, with eigenvalue $\left(\omega_\mathrm{HB}^{(k+1)}\right)^2$.
4. Repeat from step 2 until $|\omega_\mathrm{HB}^{(k+1)} - \omega_\mathrm{HB}^{(k)}| < \varepsilon$, where ε is a user-defined tolerance.

The iteration accounts for the amplitude-dependent update of the mode shape, which the proposed method omits.

In the application of Section 6.3, for each A, $\omega_{\mathrm{HB}}(q, A) - \omega_{\mathrm{I}}$ is evaluated on a uniform grid of wavenumbers close to the linear value, and the root in q is then found at the zero-crossing.

Appendix B Wavenumber-dependent linear truncation criterion

This appendix shows that the optimal retained set of fixed-interface modes generally depends on the wavenumber and that the adequacy of a given set can be assessed through the error in the reduced Bloch eigenvectors.

Let $(\omega_{\mathrm{full}}, \boldsymbol{\varphi}_{\mathrm{full}})$ denote an eigenpair of the untruncated Craig-Bampton Bloch problem ($N_{\mathrm{r}} = N_{\mathrm{i}}$), and let $(\omega, \boldsymbol{\varphi})$ denote the corresponding reduced eigenpair (obtained from Equation (38)). Let $\mathbf{B}_q$ be the Bloch operator of the untruncated model and $\widehat{\mathbf{M}}_q = \mathbf{B}_q^{\mathsf{H}} \widehat{\mathbf{M}} \mathbf{B}_q$ its Bloch mass matrix. The eigenvector error ε can be measured and controlled through the mass-weighted modal assurance criterion (MAC):

$$\mathrm{MAC} = \frac{\left| (\mathbf{E}\,\boldsymbol{\varphi})^{\mathsf{H}} \widehat{\mathbf{M}}_q \boldsymbol{\varphi}_{\mathrm{full}} \right|^2}{(\mathbf{E}\boldsymbol{\varphi})^{\mathsf{H}} \widehat{\mathbf{M}}_q (\mathbf{E}\boldsymbol{\varphi}) \;\; \boldsymbol{\varphi}_{\mathrm{full}}^{\mathsf{H}} \widehat{\mathbf{M}}_q \boldsymbol{\varphi}_{\mathrm{full}}} > 1 - \varepsilon, \tag{B5}$$

where the embedding operator

$$\mathbf{E} = \begin{bmatrix} \mathbf{I}_{N_{\mathrm{r}}} & \mathbf{0} \\ \mathbf{0} & \mathbf{0} \\ \mathbf{0} & \mathbf{I}_{N_{\mathrm{L}}} \end{bmatrix}, \qquad \mathbf{E} \begin{bmatrix} \boldsymbol{\eta}_{\mathrm{r}} \\ \mathbf{u}_{\mathrm{b}}^{\mathrm{L}} \end{bmatrix} = \begin{bmatrix} \boldsymbol{\eta}_{\mathrm{r}} \\ \mathbf{0} \\ \mathbf{u}_{\mathrm{b}}^{\mathrm{L}} \end{bmatrix}, \tag{B6}$$

lifts a reduced eigenvector to the untruncated coordinate space by padding the discarded modal coordinates with zeros. For each Bloch mode and wavenumber, N_{r} is taken as the smallest value satisfying Equation (B5), with ε a user-defined threshold. For well-separated eigenvalues, a high mass-weighted MAC generally indicates that the associated Rayleigh quotient, and hence the corresponding frequency, is also accurately reproduced.

Computing the untruncated eigenpair requires all the fixed-interface modes, which can be expensive for large models. However, the participation of a slave mode in the Bloch eigenvector decreases with its frequency, approximately as $(\omega/\omega_s)^2$. The reference eigenpair can therefore be computed with a truncated set of fixed-interface modes, such as those below ω_{cut} that are required by the promotion screen detailed in Section 4.

Notably, the order demanded by Equation (B5) is generally not uniform along a branch. Specifically, the wavenumber enters the reduced operators through the phase factors in the Bloch operator and, for a simple mass-normalized eigenpair, the eigenvalue-sensitivity relation gives [36]:

$$2\omega c_{\mathrm{g}} = \frac{\partial \omega^2}{\partial q} = \boldsymbol{\varphi}^{\mathsf{H}} \left(\frac{\partial \overline{\mathbf{K}}_q}{\partial q} - \omega^2 \frac{\partial \overline{\mathbf{M}}_q}{\partial q} \right) \boldsymbol{\varphi}. \tag{B7}$$

where $c_g = \partial\omega/\partial q$ is the group velocity. The derivatives on the right-hand side originate from the boundary coupling introduced through the Bloch reduction. Therefore, a large group velocity indicates a strong sensitivity of the mode to the phase relation between the cell boundaries.

Physically, such a mode is an extended deformation in which the propagating interface displacement actively drives the cell interior. This driven shape is not close to any single fixed-interface mode (computed with the interface held still). Thus, reproducing it requires a superposition of many of them, and the residual left by truncating that superposition grows with the strength of the boundary drive. Therefore, a larger master set is required to reach a given MAC. On flat portions of the spectrum, where $c_g \to 0$, the interior is weakly tied to the boundary phase, and a smaller master set typically suffices.

Equation (B5), followed by the promotion screen of Section 4, provides a compact candidate set at each branch-wavenumber pair. For a smooth dispersion surface, the union of these sets over the wavenumber interval is used in Section 5. An adaptive set is also possible, but changes in dimension require consistent mode tracking and normalization and can otherwise introduce artificial discontinuities.

Note that, when only a subset of the slave modes is computed, ω_{cut} depends on the retained set selected through Equation (B5), whose reference eigenpair in turn depends on ω_{cut}. In practice, the fixed-interface modes can be computed up to a trial frequency and used as reference to select the retained set through Equation (B5). If the resulting ω_{cut} is smaller than the trial frequency, the promotion screen is applied; otherwise, further modes are computed and the procedure is repeated.

Appendix C Computation of nonlinear restoring force contributions

The ratio between the nonlinear and linear forces for a given Bloch mode is computed as follows. As in Equation (45), the displacement along the prescribed Bloch orbit is $\mathbf{u}(t) = A\,\Re\big(\boldsymbol{\varphi}^{\mathrm{phys}}_{\mathrm{full},n} e^{-\mathrm{j}\omega t}\big)$, with $\omega = \omega_{\mathrm{full},n}(q)$. Each spring e, with incidence vector $\mathbf{d}_e$ (Appendix A), follows the restoring-force law of Equation (59). Along the orbit, $\Delta u_e(t) = A\,\Re\big(\Delta\varphi_e e^{-\mathrm{j}\omega t}\big)$ with $\Delta\varphi_e = \mathbf{d}_e^{\mathsf{T}}\boldsymbol{\varphi}^{\mathrm{phys}}_{\mathrm{full},n}$. The complex fundamental amplitude of f_e, defined as in Equation (47), is

$$f_{e,1} = k_e A\,\Delta\varphi_e + \frac{3}{4}\kappa_e A^3 |\Delta\varphi_e|^2 \Delta\varphi_e. \tag{C8}$$

Since the spring exerts equal and opposite forces at i_e and j_e, its projection onto $\boldsymbol{\varphi}^{\mathrm{phys}}_{\mathrm{full},n}$ is $\Delta\varphi_e^* f_{e,1}$, where * denotes complex conjugation. The ratio between the nonlinear and linear contributions, summed over all springs, is thus

$$\mu_n(q, A) = \frac{3}{4} A^2 \frac{\sum_e \kappa_e |\Delta\varphi_e|^4}{\sum_e k_e |\Delta\varphi_e|^2}. \tag{C9}$$

Since $\sum_e k_e|\Delta\varphi_e|^2 = \omega^2$ for a mass-normalized mode, μ_n coincides with the relative shift $\widetilde{\omega}^2/\omega^2 - 1$ given by Equation (48) when the full-order model is evaluated on the same orbit.

References

[1] Hussein, M.I., Leamy, M.J., Ruzzene, M.: Dynamics of phononic materials and structures: Historical origins, recent progress, and future outlook. Applied Mechanics Reviews **66**(4), 040802 (2014) https://doi.org/10.1115/1.4026911

[2] Craster, R.V., Kaplunov, J., Pichugin, A.V.: High-frequency homogenization for periodic media. Proceedings of the Royal Society A **466**, 2341–2362 (2010) https://doi.org/10.1098/rspa.2009.0612

[3] Deymier, P.A. (ed.): Acoustic Metamaterials and Phononic Crystals. Springer, ??? (2013). https://doi.org/10.1007/978-3-642-31232-8

[4] Krattiger, D., Hussein, M.I.: Bloch mode synthesis: Ultrafast methodology for elastic band-structure calculations. Physical Review E **90**(6), 063306 (2014) https://doi.org/10.1103/PhysRevE.90.063306

[5] Craig Jr, R.R., Bampton, M.C.: Coupling of substructures for dynamic analyses. AIAA journal **6**(7), 1313–1319 (1968) https://doi.org/10.2514/3.4741

[6] Krattiger, D., Hussein, M.I.: Generalized Bloch mode synthesis for accelerated calculation of elastic band structures. Journal of Computational Physics **357**, 183–205 (2018) https://doi.org/10.1016/j.jcp.2017.12.016

[7] Kim, J., Boo, S.-H., Lee, P.-S.: Considering the higher-order effect of residual modes in the Craig–Bampton method. AIAA Journal **56**(1), 403–412 (2018) https://doi.org/10.2514/1.J055666

[8] Di Gregorio, L., Lacarbonara, W.: On bandgap sensitivity to three-to-one internal resonances between acoustic and optical waves in metamaterials. Nonlinear Dynamics **113**(22), 30321–30342 (2025)

[9] Fang, X., Lacarbonara, W., Cheng, L.: Advances in nonlinear acoustic/elastic metamaterials and metastructures. Nonlinear Dynamics **113**(18), 23787–23814 (2025)

[10] Vakakis, A.F., King, M.E.: Nonlinear wave transmission in a monocoupled elastic periodic system. Journal of the Acoustical Society of America **98**(3), 1534–1546 (1995) https://doi.org/10.1121/1.413419

[11] Vakakis, A.F., Manevitch, L.I., Mikhlin, Y.V., Pilipchuk, V.N., Zevin, A.A.: Normal Modes and Localization in Nonlinear Systems. Wiley, ??? (1996)

[12] Narisetti, R.K., Leamy, M.J., Ruzzene, M.: A perturbation approach for predicting wave propagation in one-dimensional nonlinear periodic structures. Journal of Vibration and Acoustics **132**(3), 031001 (2010) https://doi.org/10.1115/1.4000775

[13] Narisetti, R.K., Ruzzene, M., Leamy, M.J.: A perturbation approach for analyzing dispersion and group velocities in two-dimensional nonlinear periodic lattices. Journal of Vibration and Acoustics **133**(6), 061020 (2011) https://doi.org/10.1115/1.4004661

[14] Narisetti, R.K., Ruzzene, M., Leamy, M.J.: Study of wave propagation in strongly nonlinear periodic lattices using a harmonic balance approach. Wave Motion **49**(2), 394–410 (2012) https://doi.org/10.1016/j.wavemoti.2011.12.005

[15] Khajehtourian, R., Hussein, M.I.: Dispersion characteristics of a nonlinear elastic metamaterial. AIP Advances **4**, 124308 (2014) https://doi.org/10.1063/1.4905051

[16] Hussein, M.I., Khajehtourian, R.: Nonlinear Bloch waves and balance between hardening and softening dispersion. Proceedings of the Royal Society A **474**, 20180173 (2018) https://doi.org/10.1098/rspa.2018.0173

[17] Campana, M.-A., Ouisse, M., Sadoulet-Reboul, E., Ruzzene, M., Neild, S., Scarpa, F.: Impact of non-linear resonators in periodic structures using a perturbation approach. Mechanical Systems and Signal Processing **135**, 106408 (2020)

[18] Palermo, A., Yousefzadeh, B., Daraio, C., Marzani, A.: Rayleigh wave propagation in nonlinear metasurfaces. Journal of Sound and Vibration **520**, 116599 (2022) https://doi.org/10.1016/j.jsv.2021.116599

[19] Hajarolasvadi, S., Celli, P., Elbanna, A., Daraio, C.: Experimental evidence of amplitude-dependent surface wave dispersion. Applied Physics Letters **123**(8), 081704 (2023) https://doi.org/10.1063/5.0151294

[20] Rosenberg, R.M.: On nonlinear vibrations of systems with many degrees of freedom. Advances in Applied Mechanics **9**, 155–242 (1966) https://doi.org/10.1016/S0065-2156(08)70008-5

[21] Shaw, S.W., Pierre, C.: Non-linear normal modes and invariant manifolds. Journal of Sound and Vibration **150**(1), 170–173 (1991) https://doi.org/10.1016/0022-460X(91)90412-D

[22] Pesheck, E., Boivin, N., Pierre, C., Shaw, S.W.: Nonlinear modal analysis of structural systems using multi-mode invariant manifolds. Nonlinear Dynamics **25**, 183–205 (2001) https://doi.org/10.1023/A:1012910918498

[23] Jiang, D., Pierre, C., Shaw, S.: The construction of non-linear normal modes for

systems with internal resonance. International Journal of Non-Linear Mechanics **40**(5), 729–746 (2005) https://doi.org/10.1016/j.ijnonlinmec.2004.08.010

[24] Peeters, M., Viguié, R., Sérandour, G., Kerschen, G., Golinval, J.-C.: Nonlinear normal modes, part ii: Toward a practical computation using numerical continuation techniques. Mechanical Systems and Signal Processing **23**(1), 195–216 (2009) https://doi.org/10.1016/j.ymssp.2008.04.003

[25] Touzé, C., Amabili, M.: Nonlinear normal modes for damped geometrically nonlinear systems: Application to reduced-order modelling. Journal of Sound and Vibration **298**(4-5), 958–981 (2006) https://doi.org/10.1016/j.jsv.2006.07.011

[26] Touzé, C., Vizzaccaro, A., Thomas, O.: Model order reduction methods for geometrically nonlinear structures: A review. Nonlinear Dynamics **105**, 1141–1190 (2021) https://doi.org/10.1007/s11071-021-06693-9

[27] Haller, G., Ponsioen, S.: Nonlinear normal modes and spectral submanifolds: Existence, uniqueness and use in model reduction. Nonlinear Dynamics **86**, 1493–1534 (2016) https://doi.org/10.1007/s11071-016-2974-z

[28] Ponsioen, S., Jain, S., Haller, G.: Model reduction to spectral submanifolds and forced-response calculation in high-dimensional systems. Journal of Sound and Vibration **488**, 115640 (2020) https://doi.org/10.1016/j.jsv.2020.115640

[29] Jain, S., Haller, G.: How to compute invariant manifolds and their reduced dynamics in high-dimensional finite element models. Nonlinear Dynamics **107**, 1415–1450 (2022) https://doi.org/10.1007/s11071-021-06957-4

[30] Wang, T., Touzé, C., Li, H., Ding, Q.: Normal form computation of nonlinear dispersion relationship for locally resonant metamaterial. Physica D: Nonlinear Phenomena **488**, 135115 (2026) https://doi.org/10.1016/j.physd.2026.135115

[31] Quqa, S., Marzani, A., Palermo, A.: Reduced-order modeling for dispersion analysis of elastic waveguides coupled to arrays of nonlinear systems. Journal of Sound and Vibration **618**, 119256 (2025) https://doi.org/10.1016/j.jsv.2025.119256

[32] Pesheck, E., Pierre, C., Shaw, S.W.: A new Galerkin-based approach for accurate non-linear normal modes through invariant manifolds. Journal of sound and vibration **249**(5), 971–993 (2002) https://doi.org/10.1006/jsvi.2001.3914

[33] Farzbod, F., Leamy, M.J.: The treatment of forces in Bloch analysis. Journal of Sound and Vibration **325**(3), 545–551 (2009) https://doi.org/10.1016/j.jsv.2009.03.035

[34] COMSOL, Inc.: COMSOL Multiphysics® V. 5.6. Stockholm, Sweden (2026). https://www.comsol.com

[35] Setio, S., Setio, H.D., Jezequel, L.: Modal analysis of nonlinear multi-degree-of-freedom structure. The International Journal of Analytical and Experimental Modal Analysis **7**(2), 75–93 (1992)

[36] Bhaskar, A.: Group velocity of elastic waves as eigensensitivity of a parameter dependent eigenvalue problem. International Journal of Mechanical Sciences **55**(1), 42–49 (2012) https://doi.org/10.1016/j.ijmecsci.2011.12.001